Electronic Supplementary Material (ESI) for ChemComm.

Supporting Information

Asymmetric [N-I-N]$^+$ Halonium Complexes

Jas S. Ward,[a] Giorgia Fiorini,[a] Antonio Frontera[b] and Kari Rissanen[a]

[a] University of Jyvaskyla, Department of Chemistry,

40014, Jyväskylä, Finland

[b]Department de Química, Universitat de les Illes Balears, Palma de Mallorca, Baleares, Spain

Contents

1. Synthesis

1.1 General Information

All reagents and solvents were obtained from commercial suppliers and used without further purification. For structural NMR assignments, ^{1}H NMR spectra were recorded on a Bruker Avance 300 MHz spectrometer at 25ºC in CD_2Cl_2. The ^{1}H-^{15}N NMR correlation spectra were recorded on a Bruker Avance III 500 MHz spectrometer at 25ºC in CD_2Cl_2. Chemical shifts are reported on the δ scale in ppm using the residual solvent signal as internal standard (CD_2Cl_2; δ_H 5.32), or for ^{1}H-^{15}N NMR spectroscopy, to an external *d*$_3$-$MeNO_2$ standard. For ^{1}H NMR spectroscopy, each resonance was assigned according to the following conventions: chemical shift (δ) measured in ppm, observed multiplicity, number of hydrogens, observed coupling constant (*J* Hz), and assignment. Multiplicities are denoted as: s (singlet), d (doublet), t (triplet), q (quartet) m (multiplet) and br (broad). Complexes **1a** and **2a** were prepared according to literature procedures.[1]

1.2 Synthesis and Characterisation: silver(I) complexes

Scheme 1. Synthesis of silver(I) complexes 1b, 1c, 1d and 1e

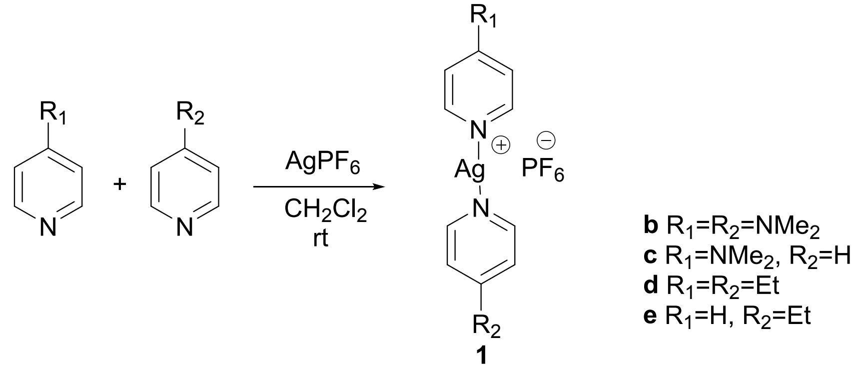

Bis(4-dimethylaminopyridine)silver(I) hexafluorophosphate (**1b**)

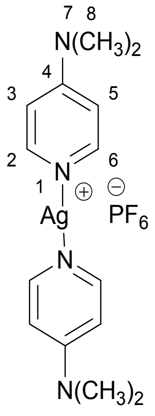

1b

In a 10 mL vial, $AgPF_6$ (12.64 mg, 0.05 mmol) was weighed out and equipped with a magnetic stirring bar, followed by CH_2Cl_2 (1.0 mL). Subsequently, a solution of 4-(dimethylamino)pyridine (12.22 mg, 0.10 mmol) in CH_2Cl_2 (2.0 mL) was added at room temperature. The resulting reaction mixture was stirred for 2 hours, then all volatiles removed by evaporation to leave a white solid. Single crystals of a quality suitable for X-ray diffraction were obtained by vapour diffusion from three different systems (CH_2Cl_2/pentane, dichloroethane/pentane, and MeOH/toluene). Yield = 21.2 mg (85%).

^1H NMR (300 MHz, CD_2Cl_2): δ 8.04-8.07 (m, 4H, H2 and H6), 6.61-6.64 (m, 4H, H3 and H5), 3.08 (s, 12H, 4 x CH_3); ^1H-^{15}N correlation NMR (500 MHz, CD_2Cl_2): δ -316.0 (N7), -169.8 (N1). Analysis Found: C, 35.04; H, 4.27: N, 11.53%. Calculated for $C_{14}H_{20}AgF_6N_4P\cdot 0.1(C_7H_{10}N_2)$: C, 34.66; H, 4.16: N, 11.55%.*

---

* A minor 4-DMAP impurity was consistently observed in the elemental analysis results for compound **1b**.

(4-dimethylaminopyridine)(pyridine)silver(I) hexafluorophosphate (**1c**)

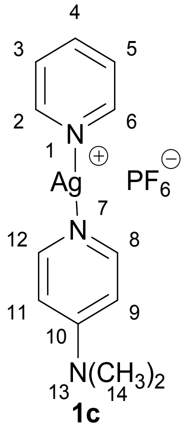

1c

In a 10 mL vial, $AgPF_6$ (12.64 mg, 0.05 mmol) and 4-(dimethylamino)pyridine (6.10 mg, 0.05 mmol) were weighed out. Subsequently, a solution of pyridine (4.04 µL, 0.05 mmol) and CH_2Cl_2 (3.0 mL) was added at room temperature. The resulting reaction mixture stirred for 5 min, until all solids disappeared, then all volatiles removed by evaporation to leave a white solid. Yield = 19.8 mg (87%).

Single crystals of a quality suitable for X-ray diffraction were obtained by vapour diffusion of CH_2Cl_2/pentane.

^1H NMR (300 MHz, CD_2Cl_2): δ 8.58 (d, 2H, ^2J = 4.86 Hz, H2 and H6), 8.05 (d, 2H, ^2J = 6.42 Hz, H8 and H12), 7.93 (tt, 1H, ^2J = 7.73 Hz, ^3J = 1.69 Hz, H4), 7.50-7.53 (m, 2H, H3 and H5), 6.61-6.63 (m, 2H, H9 and H11), 3.07 (s, 3H, CH_3); ^1H-^{15}N correlation NMR (500 MHz, CD_2Cl_2): δ -315,0 (N13), -173.7 (N7), -113.8 (N1). Analysis Found: C, 32.18; H, 3.49: N, 9.42%. Calculated for $C_{12}H_{15}AgF_6N_3P$: C, 31.74; H, 3.33; N, 9.25%.

Bis(4-ethylpyridine)silver(I) tetrafluoroborate (**1d**)

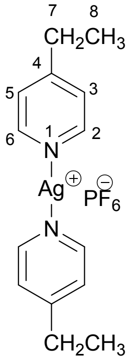

1d

In a 10 mL vial, $AgPF_6$ (12.64 mg, 0.05 mmol) was weighed out and equipped with a magnetic stirring bar, followed by CH_2Cl_2 (1.0 mL). Subsequently, a solution of 4-ethylpyridine in CH_2Cl_2 (11.34 µL in 2.0 mL) was added at room temperature. The resulting reaction mixture stirred for 2 hours, then all volatiles were removed by evaporation to leave a white solid. Single crystals of a quality suitable for X-ray diffraction were obtained by evaporation of CH_2Cl_2. Yield = 18.1 mg (78%)

^{1}H NMR (300 MHz, CD_2Cl_2): δ 8.44 (d, 4H, ^2J = 5.3 Hz, H2 and H6), 7.35 (d, 4H, ^2J = 5.3 Hz, H3 and H5), 2.73 (q, 4H, ^2J = 7.3 Hz, H7), 1.28 (t, 6H, H8); ^{1}H-^{15}N correlation NMR (500 MHz, CD_2Cl_2): δ -119,7 (N1). Analysis Found: C, 36.23; H, 4.00: N, 5.88%. Calculated for $C_{14}H_{18}AgF_6N_2P$: C, 36.00; H, 3.88; N, 6.00%.

(4-ethylpyridine)(pyridine)silver(I) tetrafluoroborate (**1e**)

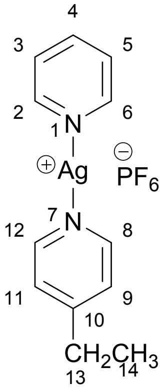

1e

In a 10 mL, $AgPF_6$ (12.64 mg, 0.05 mmol) was weighed out and a magnetic stirring bar added. Subsequently, a solution of pyridine (4.04 μL, 0.05 mmol) and 4-ethylpyridine (5.67 μL, 0.05 mmol) in CH_2Cl_2 (3.0 mL) was added at room temperature. The resulting reaction mixture stirred for 5 minutes, until all solids disappeared, then all volatiles were removed by evaporation to leave a white solid. Single crystals of a quality suitable for X-ray diffraction were obtained by vapour diffusion of CH_2Cl_2/^{t}BuOMe. Yield = 19.4 mg (89%).
^{1}H NMR (300 MHz, CD_2Cl_2): δ 8.62 (d, 2H, ^2J = 4.27 Hz, H2 and H6), 8.49 (d, 2H, ^2J = 5.84 Hz, H8 and H12), 7.95 (t, 1H, ^2J = 7.42 Hz, H4), 7.55 (t, 2H, ^2J = 6.89 Hz, H3 and H5), 7.41 (d, 2H, ^2J = 5.31 Hz, H9 and H11), 2.76 (q, 2H, ^2J = 6.89 Hz, H13), 1.29 (t, 3H, ^2J = 7.43 Hz, H14); ^{1}H-^{15}N correlation NMR (500 MHz, CD_2Cl_2): δ -131.5 (N7), -116.8 (N1). Analysis Found: C, 33.28; H, 3.31: N, 6.40%. Calculated for $C_{12}H_{14}AgF_6N_2P$: C, 32.83; H, 3.21; N, 6.38%.

1.3 Synthesis and Characterisation: iodine(I) complexes

Scheme 2. Synthesis of iodine(I) complexes 2b, 2c, 2d and 2e

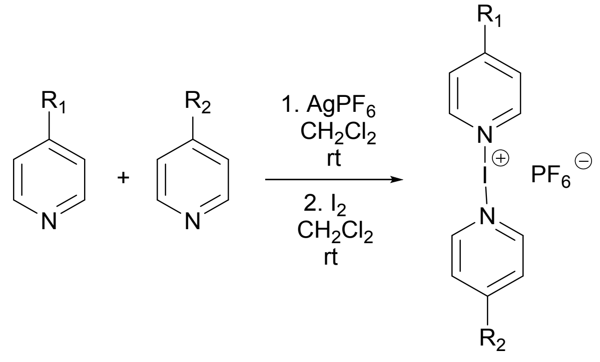

2

b R_1=R_2=NMe$_2$
c R_1=H, R_2=NMe$_2$
d R_1=R_2=Et
e R_1=H, R_2=Et

Bis(4-dimethylaminopyridine)iodine(I) hexafluorophosphate (**2b**)

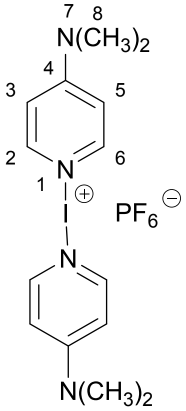

2b

In a 10 mL vial, $AgPF_6$ (12.64 mg, 0.05 mmol) was weighed out and equipped with a stirring bar, followed by CH_2Cl_2 (1.0 mL). Subsequently, a solution of 4-(dimethylamino)pyridine (12.22 mg, 0.10 mmol) in CH_2Cl_2 (2.0 mL) was added at room temperature and the resulting reaction mixture stirred for 2 hours. In another vial, I_2 (27.6 mg, 0.05 mmol) was dissolved in CH_2Cl_2 (1.0 mL) and then added to the reaction mixture. Immediately upon the addition, light yellow AgI was precipitated, and stirring was continued for 30 minutes. All volatiles were removed by evaporation to leave an off-white solid. Single crystals of a quality suitable for X-ray diffraction were obtained by evaporation from CH_2Cl_2. Yield = 19.3 mg (75%).

The ^1H NMR spectrum was consistent with that previously reported in the literature.[2] ^1H NMR (300 MHz, CD_2Cl_2): δ 8.04 (d, 4H, H2 and H6), 6.48 (d, 4H, ^3J = 6.49 Hz, H3 and H5), 3.09 (s, 6H, 2 x CH_3); ^1H-^{15}N correlation NMR (500 MHz, CD_2Cl_2): δ -309.1 (N7), -217.8 (N1).

(4-dimethylaminopyridine)(pyridine)iodine(I) hexafluorophosphate (**2c**)

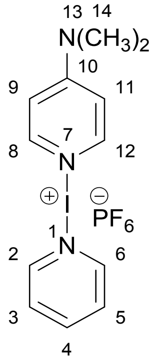

2c

In a 10 mL vial, $AgPF_6$ (12.64 mg, 0.05 mmol) and 4-(dimethylamino)pyridine (6.10 mg, 0.05 mmol) were weighed out and a magnetic stirring bar was added. Subsequently, a solution of pyridine (4.04 µL, 0.05 mmol) and CH_2Cl_2 (3.0 mL) was added at room temperature. The resulting reaction mixture stirred for 5 minutes, until all solids disappeared. In another vial, I_2 (17.1 mg, 0.05 mmol) was dissolved in CH_2Cl_2 (1.0 mL), and was then added to the reaction mixture. Immediately upon the addition, light yellow AgI was precipitated. Stirring was continued for 30 minutes. Single crystals of a quality suitable for X-ray diffraction were obtained by vapour diffusion of CH_2Cl_2/pentane.

The reported ^1H and ^1H-^{15}N correlation NMR spectra represent a mixture of **2a**, **2b**, and **2c**. Due to the overlapping nature of the signals, the integrals have not been evaluated. ^1H NMR (300 MHz, CD_2Cl_2): 8.75-8.76 (m, H2 and H6 from **2a**), 8.66 (br, H2 and H6 from **2c**), 8.22 (m, H4 from **2a**), 8.05-8.10 (*signals overlapping*; H2 and H6 from **2b**; H4, H8 and H12 from **2c**), 7.62 (m, H3 and H5 from **2a**), 7.55 (br, H3 and H5 from **2c**), 6.49-6.54 (*signals overlapping*; H3 and H5 from **2b**; H9 and H10 from **2c**), 3.10-3.14 (*signals overlapping*; 2 x CH_3 from **2b** and **2c**). ^1H-^{15}N correlation NMR (500 MHz, CD_2Cl_2): δ -307.2 (N7 from **2b**), -304.2 (N13 from **2c**), -237.6 (N7 from **2c**), -217.7 (N1 from **2b**).[‡]

[‡] Due to the low concentration, the ^1H-^{15}N NMR spectroscopy correlations of compound **2a** and the pyridine nitrogen of compound **2c** were not observed.

Bis(4-ethylpyridine)iodine(I) hexafluorophosphate (**2d**)

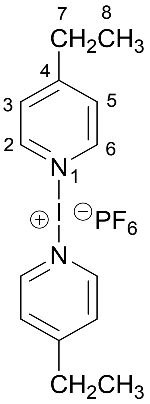

2d

In a 10 mL vial, $AgPF_6$ (12.64 mg, 0.05 mmol) was weighed out and a magnetic stirring bar added. Subsequently, 4-ethylpyridine (11.34 µL, 0.1 mmol) in CH_2Cl_2 (3.0 mL) was added at room temperature, and the resulting reaction mixture was stirred for 2 hours. In another vial, I_2 (86.6 mg, 0.34 mmol) was dissolved in CH_2Cl_2 (2.0 mL). The I_2 solution (0.294 mL) was then added to the reaction mixture, and immediately upon addition, light yellow AgI was precipitated. Stirring was continued for 30 min, at which point the reaction had occurred but was not complete, as a small amount of **1d** was still visible in the NMR.[**] Yield = 16.2 mg (67%).

^{1}H NMR (300 MHz, CD_2Cl_2): 8.58 (d, 4H, ^2J = 6.05 Hz, H2 and H6), 7.41 (d, 4H, ^2J = 6.04 Hz, H3 and H5), 2.82 (q, 4H, ^2J = 7.38 Hz, H7), 1.25-1.32 (m, 9H, H8). ^{1}H-^{15}N correlation NMR (500 MHz, CD_2Cl_2): δ -182.9 (N1).

[**] Longer reaction times were attempted, but 30 minutes was found to be optimal, as longer times only caused an increase of the impurity present (as determined by monitoring using ^{1}H NMR spectroscopy).

(4-ethylpyridine)(pyridine)iodine(I) hexafluorophosphate (**2e**)

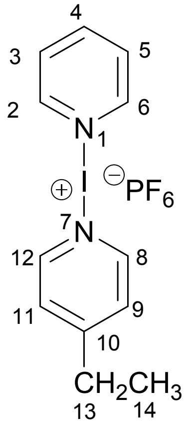

2e

In a 10 mL vial, $AgPF_6$ (12.64 mg, 0.05 mmol) was weighed out and a magnetic stirring bar added. Subsequently, a solution of pyridine (4.04 µL, 0.05 mmol) and 4-ethylpyridine (5.67 µL, 0.05 mmol) in CH_2Cl_2 (3.0 mL) was added at room temperature. The resulting reaction mixture was stirred for 5 minutes, until all solids disappeared. In another vial, I_2 (86.6 mg, 0.34 mmol) was dissolved in CH_2Cl_2 (2.0 mL). The I_2 solution (0.294 mL) was then added to the reaction mixture, and immediately upon addition, light yellow AgI was precipitated. Stirring was continued for 30 minutes.

The reported ^{1}H NMR spectra and ^{1}H-^{15}N correlation NMR represent a mixture of **2d** and **2e**. Due to the overlapping nature of the signals, the integrals have not been evaluated.

^{1}H NMR (300 MHz, CD_2Cl_2): 8.73-8.76 (m, H2 and H6, **2e**), 8.57-8.60 (*overlapping signals*; H8 and H12 from **2e**; H2 and H6 from **2d**), 8.20 (t, ^3J = 8.05 Hz, H4 from **2e**), 7.59-7.64 (m, H3 and H5 from **2e**), 7.40-7.42 (*overlapping signals*; H9 and H11 from **2e**; H3 and H5 from **2d**), 2.80-2.86 (m, H13 from **2e**; H7 from **2d**), 1.30 (t, ^3J = 7.38 Hz, H14 from **2e**; H8 from **2d**); ^{1}H-^{15}N correlation NMR (500 MHz, CD_2Cl_2): δ -185.9 (N7 from **2e**), -182.4 (N1 from **2d**), -172.0 (N1 from **2e**).

2. NMR Measurements

2.1 Comparison of ^{15}N NMR spectroscopy

	Uncomplexed	**[AgL$_2$]PF$_6$**		**[IL$_2$]PF$_6$**	
py	-67.7	**1a**	-122.7	**2a**	-176.6
4-DMAP		**1b**		**2b**	
NMe$_2$	-328.7		-316.0		-309.1
N(ring)	-108.9		-169.8		-217.8
NMe$_2$		**1c**	-315.0	**2c**	-304.2
N(4-DMAP)			-173.7		-237.6
N(py)			-113.8		§
4-Etpy	-75.6	**1d**	-119.7	**2d**	-182.9
N(4-Etpy)		**1e**	-131.5	**2e**	-185.9
N(py)			-116.8		-172.0

All values in ppm.

§ The N(py) peak for **2c** was not observed due to the low concentration of the sample.

2.2 ^{1}H NMR spectra of Synthesised Complexes

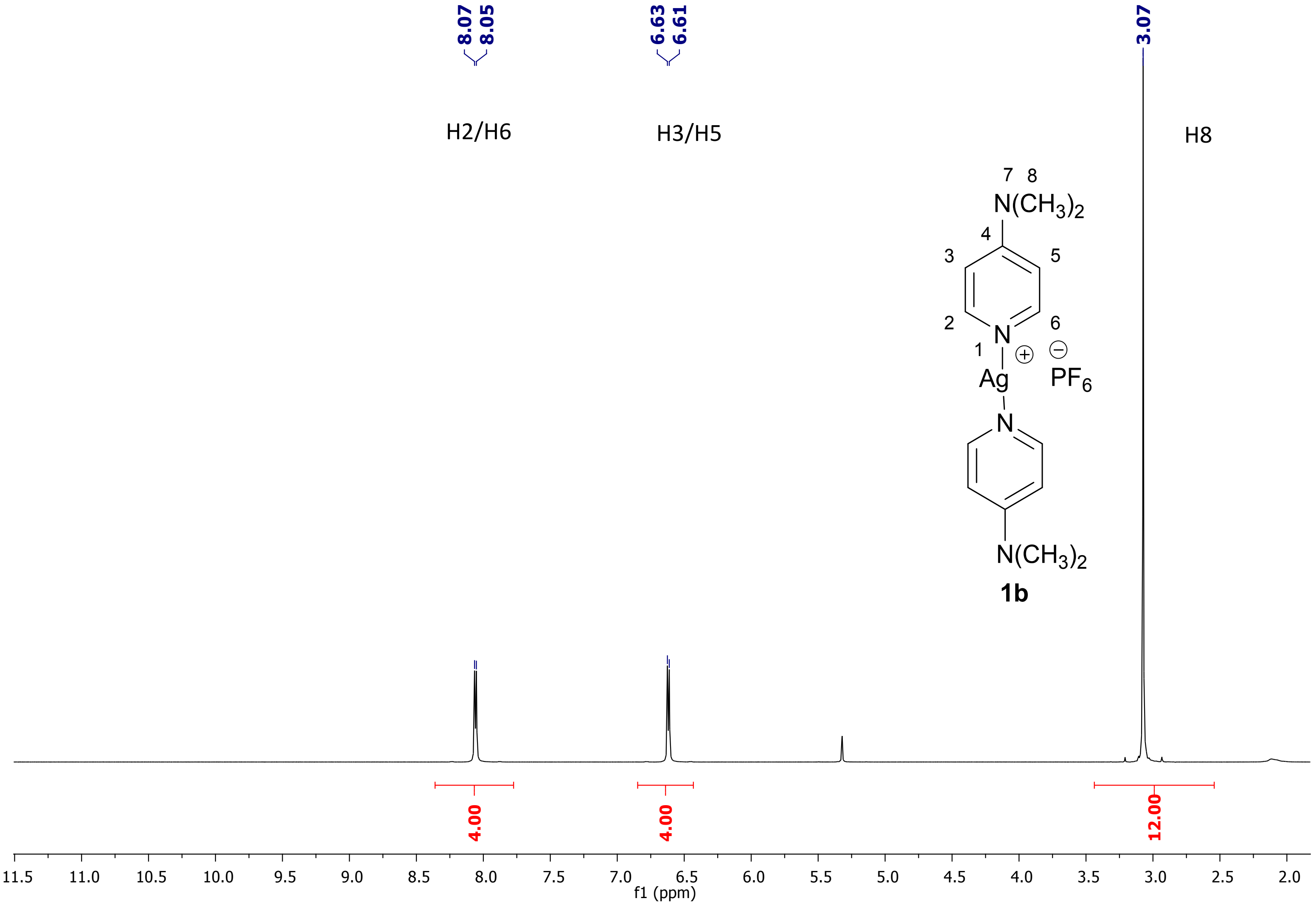

Figure S1. The ^{1}H NMR spectra of $[Ag(4\text{-}DMAP)_2]PF_6$ (1b).

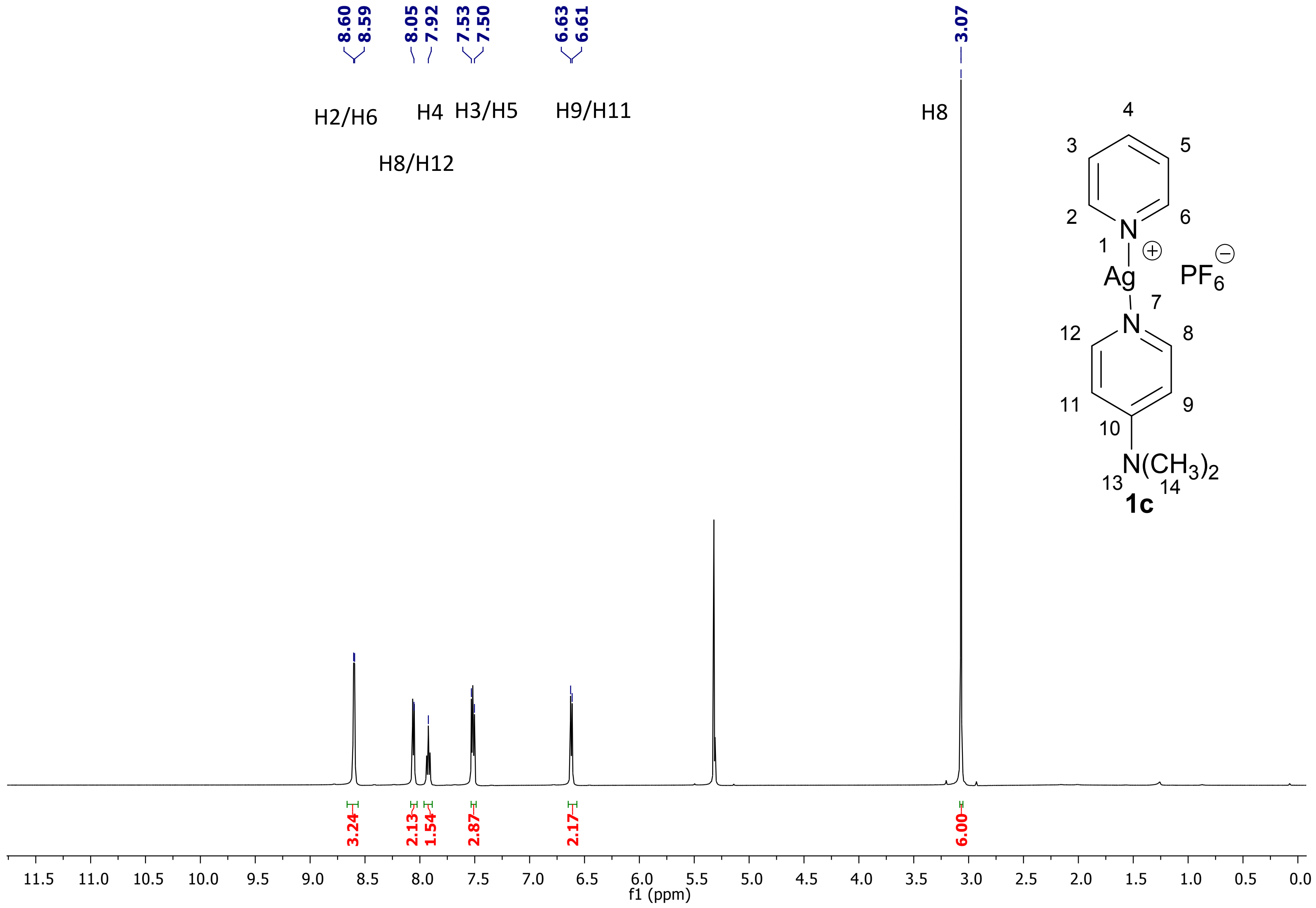

Figure S2. The ^{1}H NMR spectra of [Ag(4-DMAP)(py)]PF$_6$ (1c).

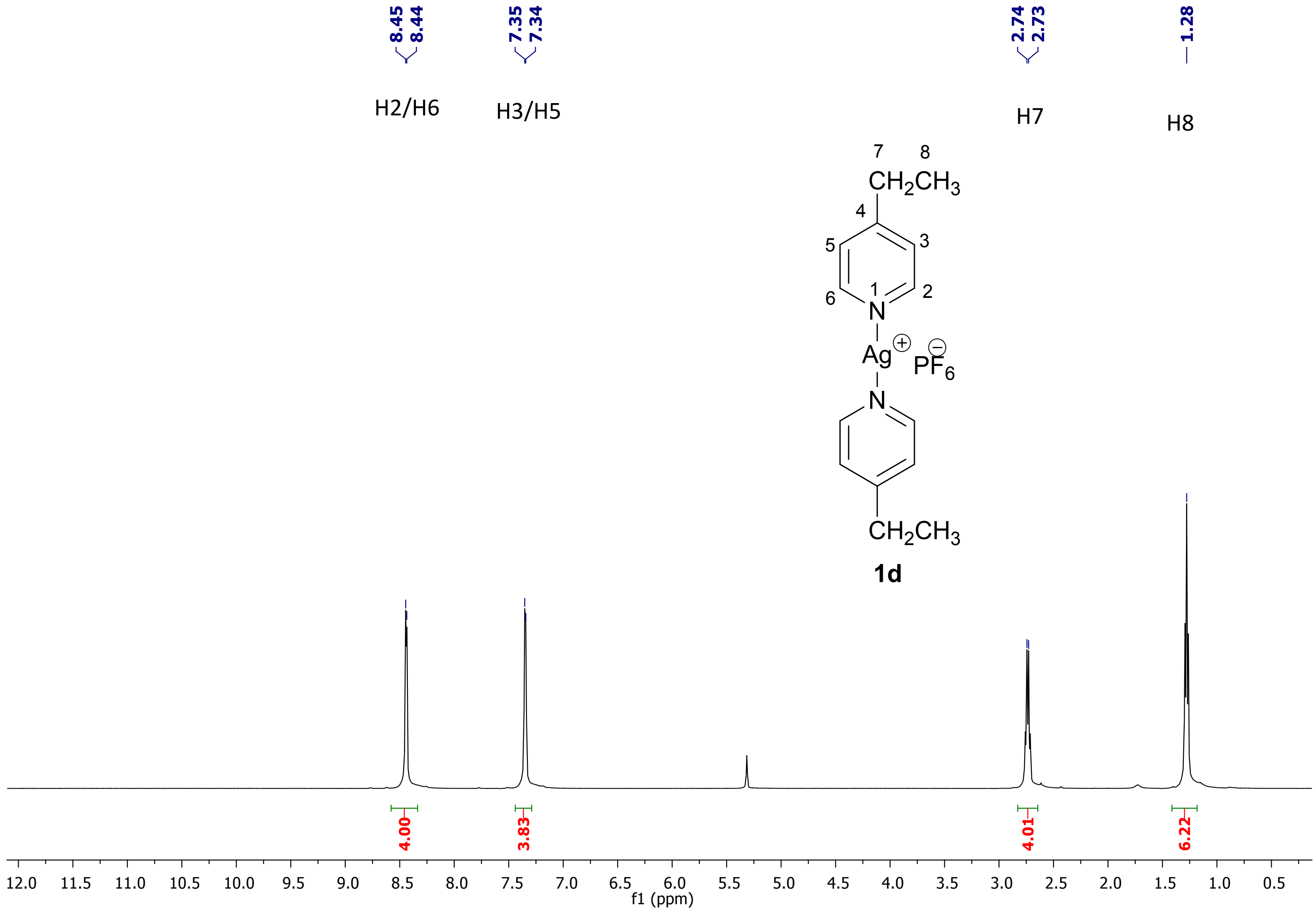

Figure S3. The ^{1}H NMR spectra of [Ag(4-Etpy)$_2$]PF$_6$ (1d).

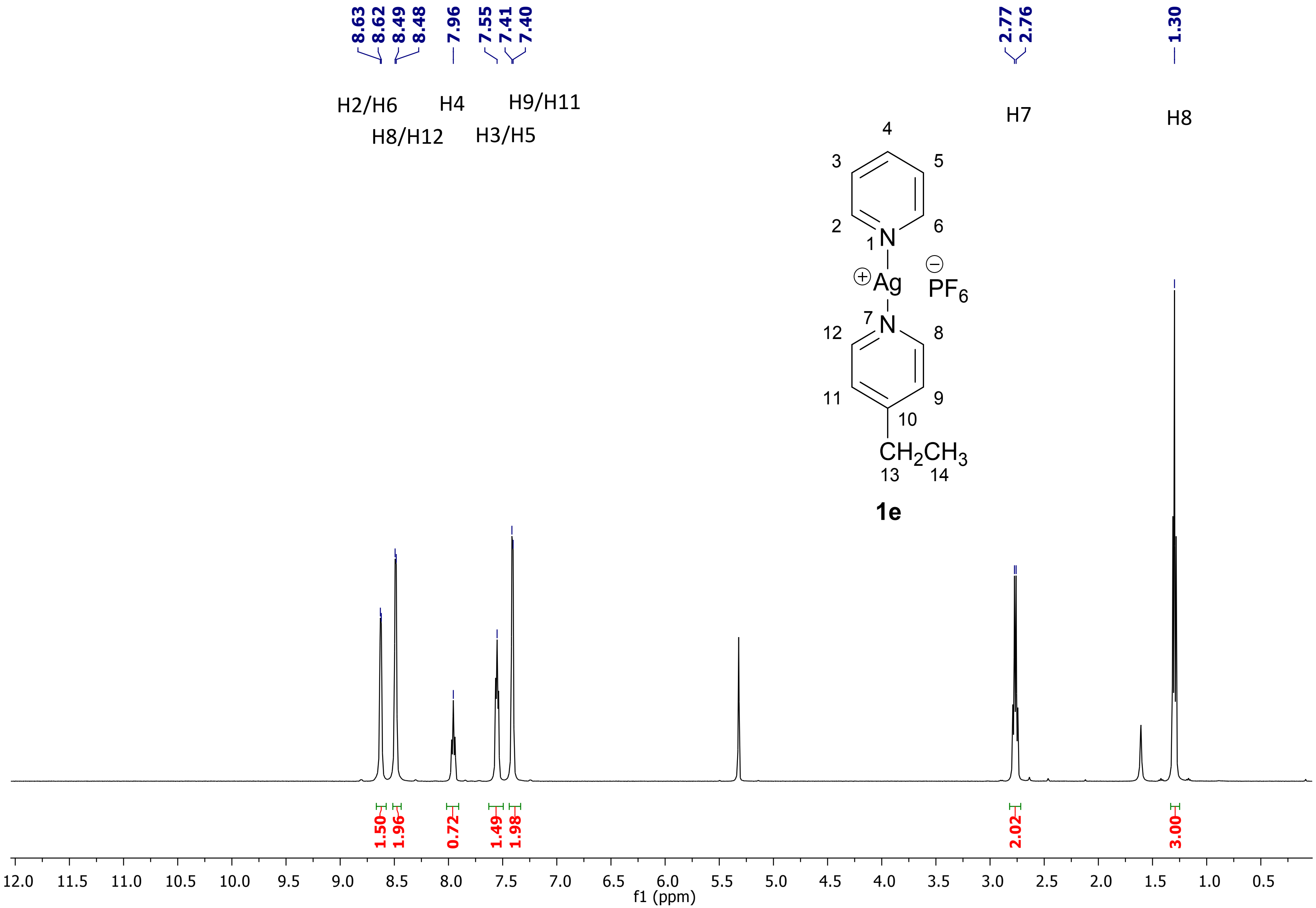

Figure S4. The ^{1}H NMR spectra of [Ag(4-Etpy)(py)]PF$_6$ (1e).

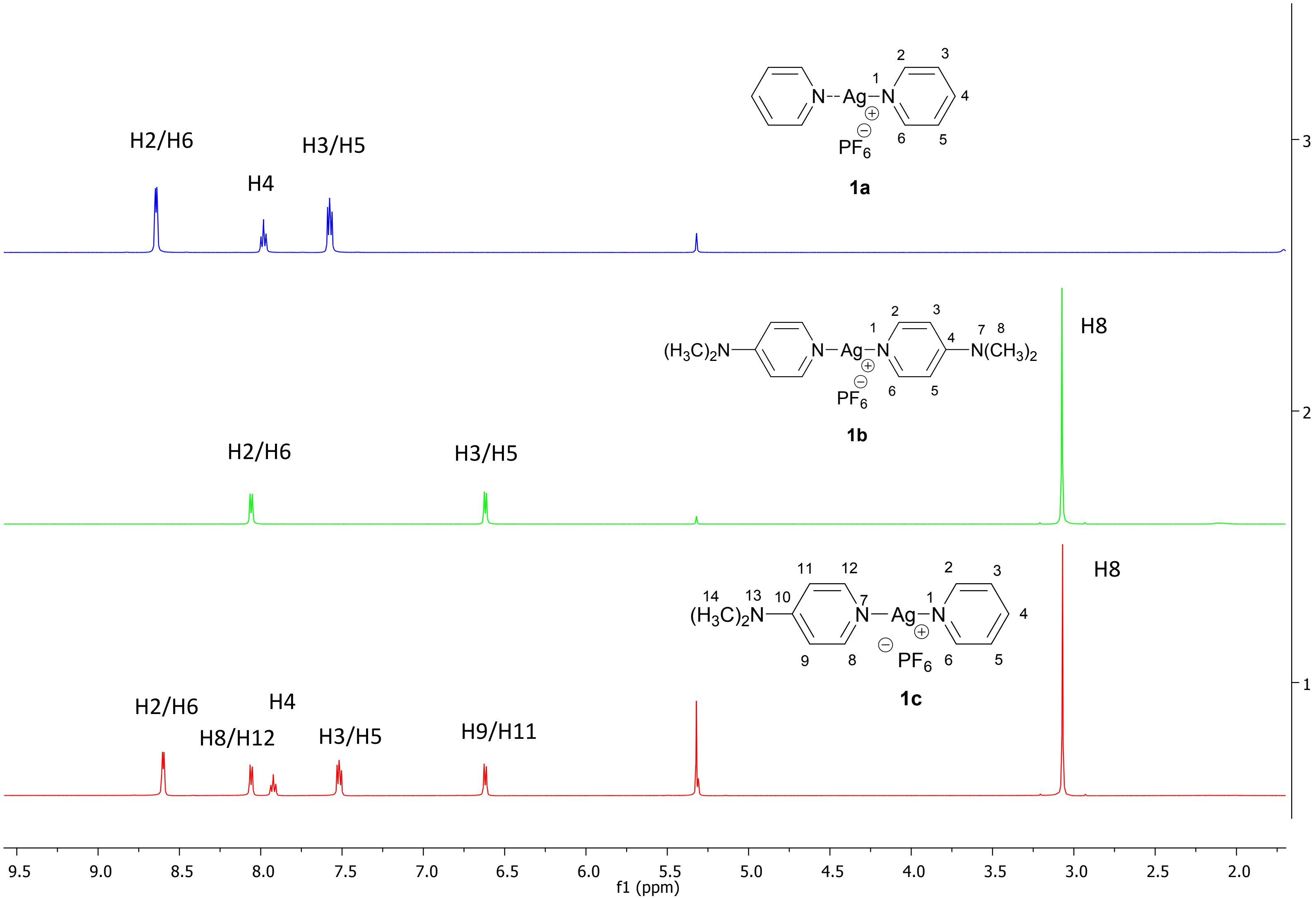

Figure S5. The compared ^{1}H NMR spectra of 1a, 1b and 1c (in CD_2Cl_2).

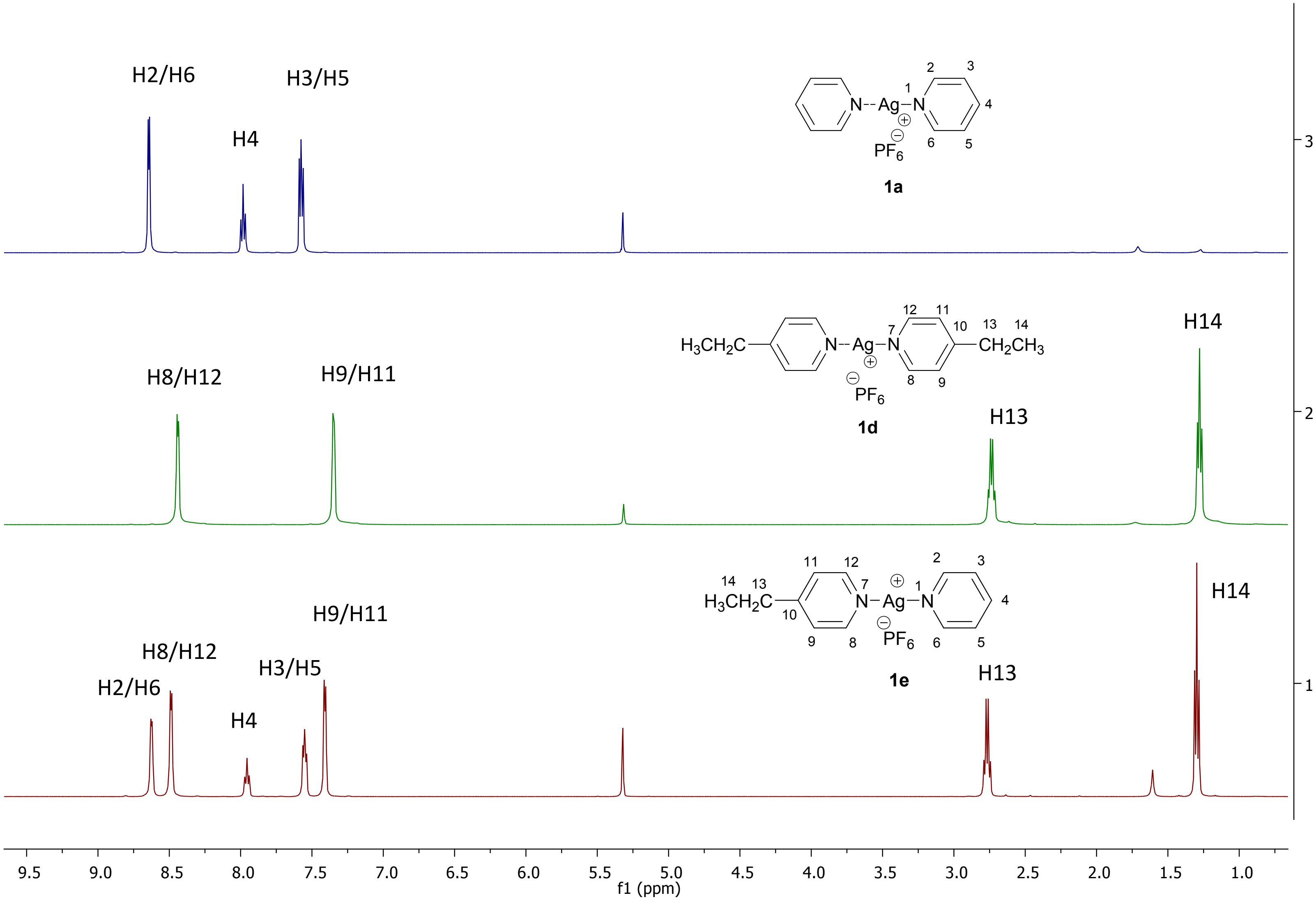

Figure S6. The compared ^{1}H NMR spectra of 1a, 1d and 1e (in CD_2Cl_2).

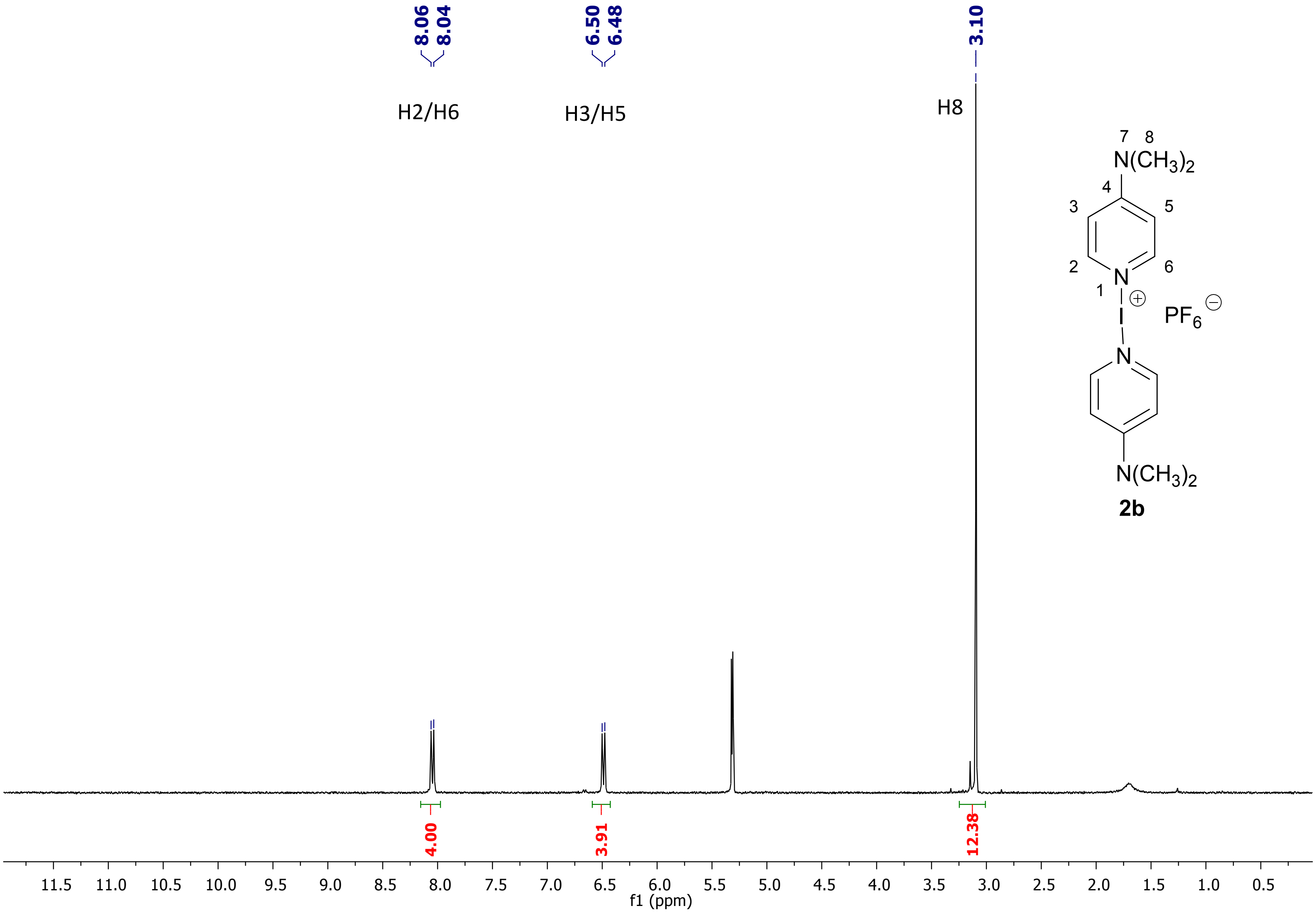

Figure S7. The ^{1}H NMR spectra of [I(4-DMAP)$_2$]PF$_6$ (2b).

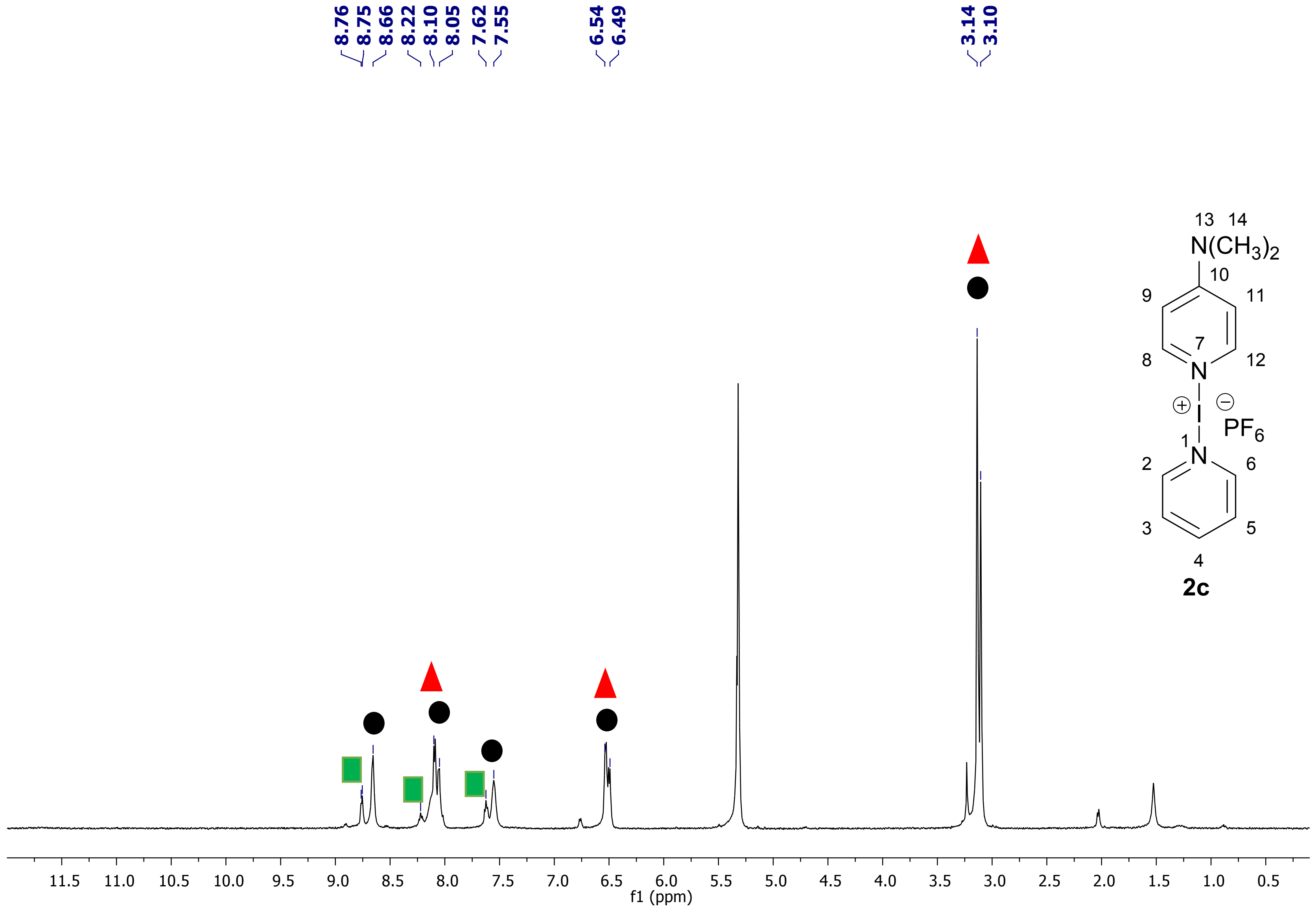

Figure S8. The ^{1}H NMR spectra of [I(py)(4-DMAP)]PF$_6$ (2c) (Colour Key: green square = 2a, red triangle = 2b, black circle = 2c).

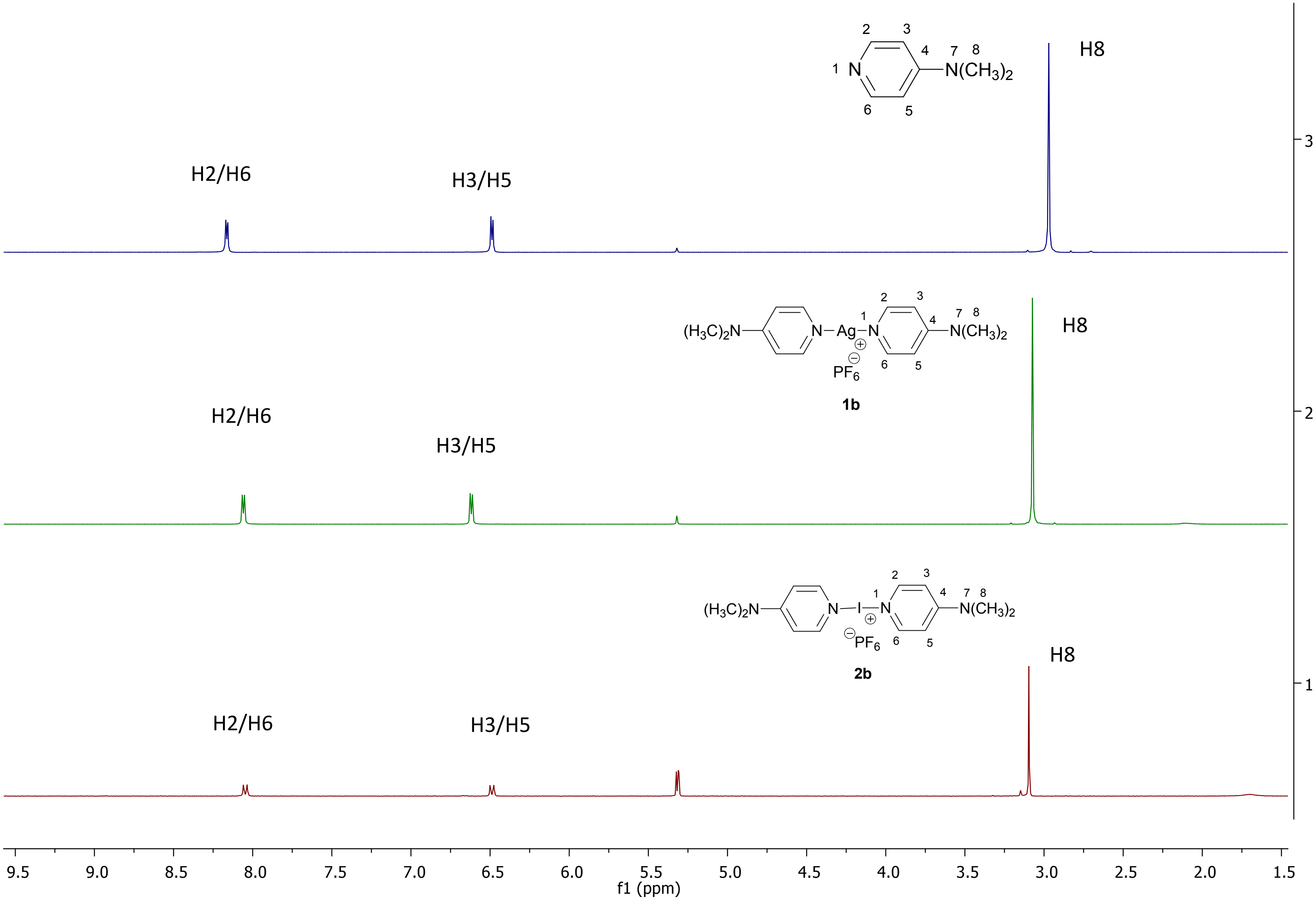

Figure S9. The compared ^{1}H NMR spectra of 4-DMAP, 1b and 2b (in CD_2Cl_2).

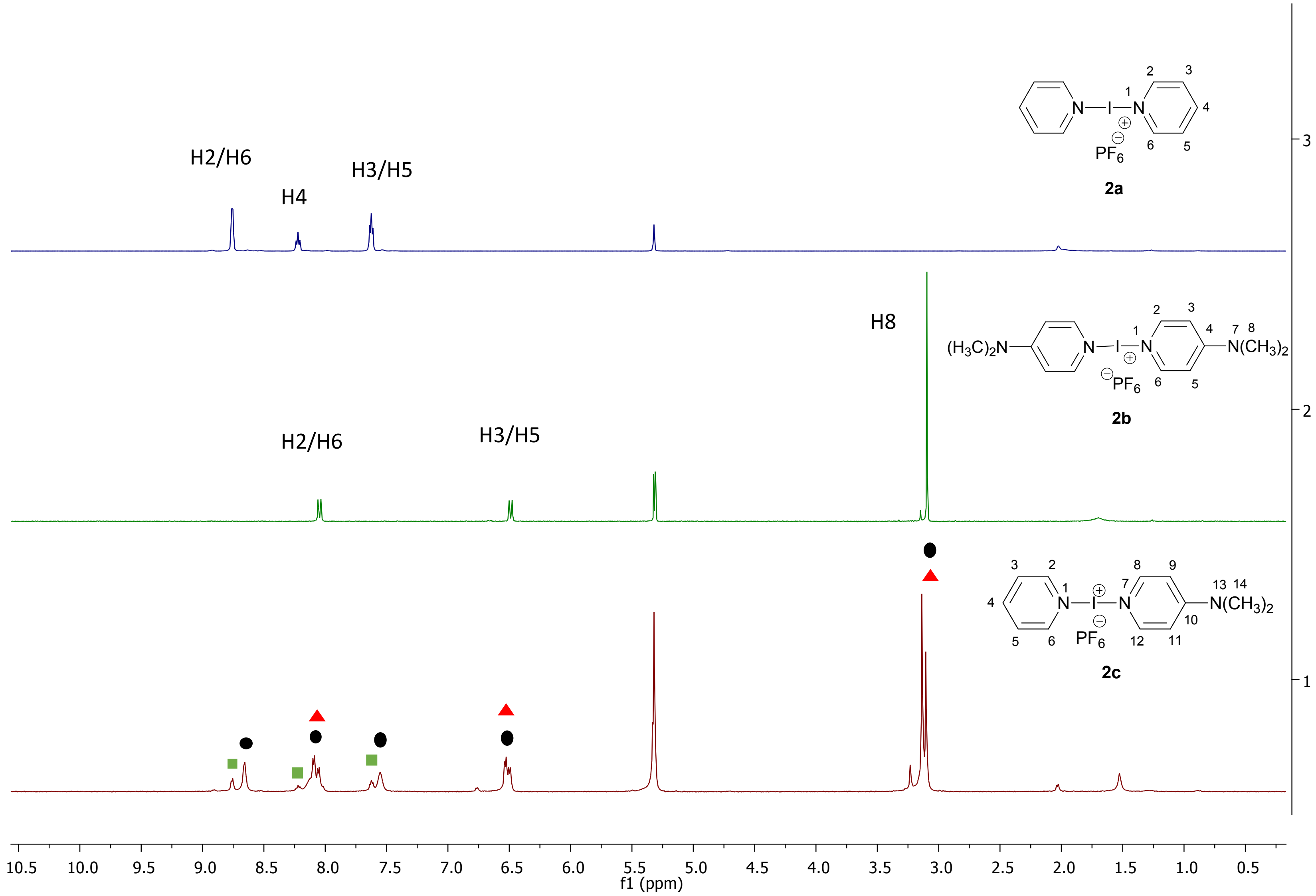

Figure S10. The compared ^1H NMR spectra of 2a, 2b and 2c (in CD_2Cl_2) (Colour Key: green square = 2a, red triangle = 2b, black circle = 2c).

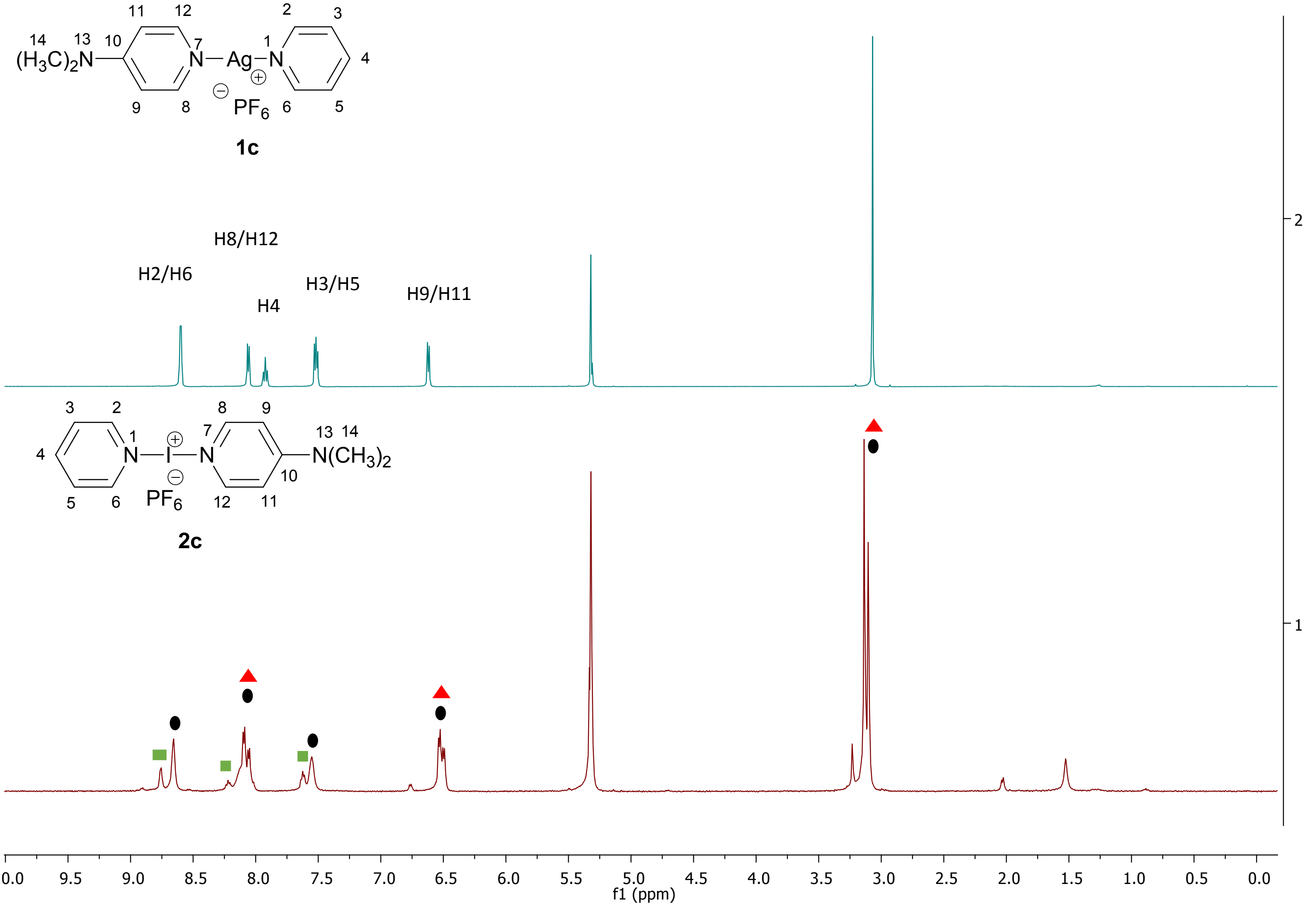

Figure S11. The compared ^{1}H NMR spectra of 1c and 2c (in CD$_2$Cl$_2$) (Colour Key: green square = 2a, red triangle = 2b, black circle = 2c).

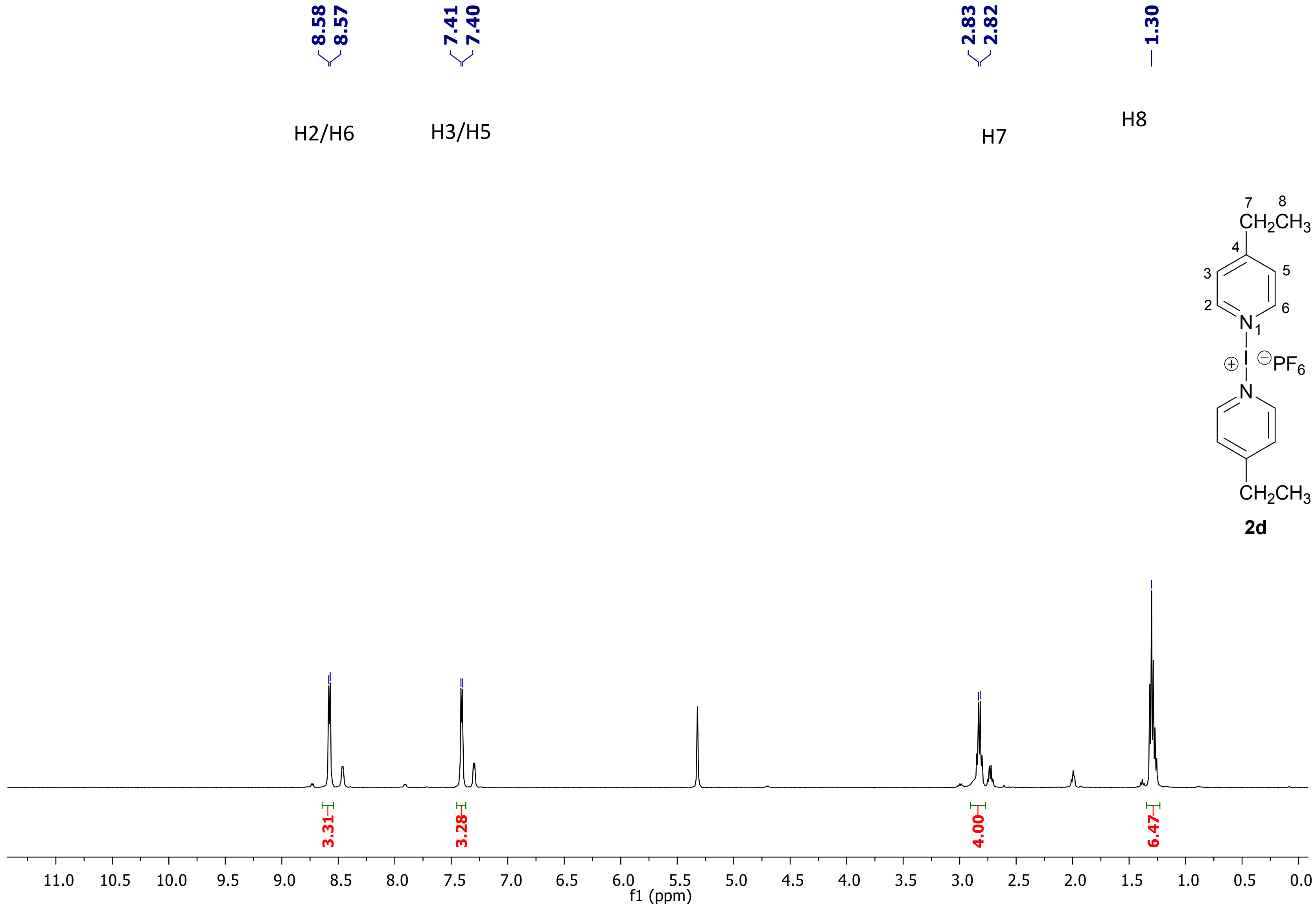

Figure S12. The ^1H NMR spectra of $[I(4\text{-}Etpy)_2]PF_6$ (2d).

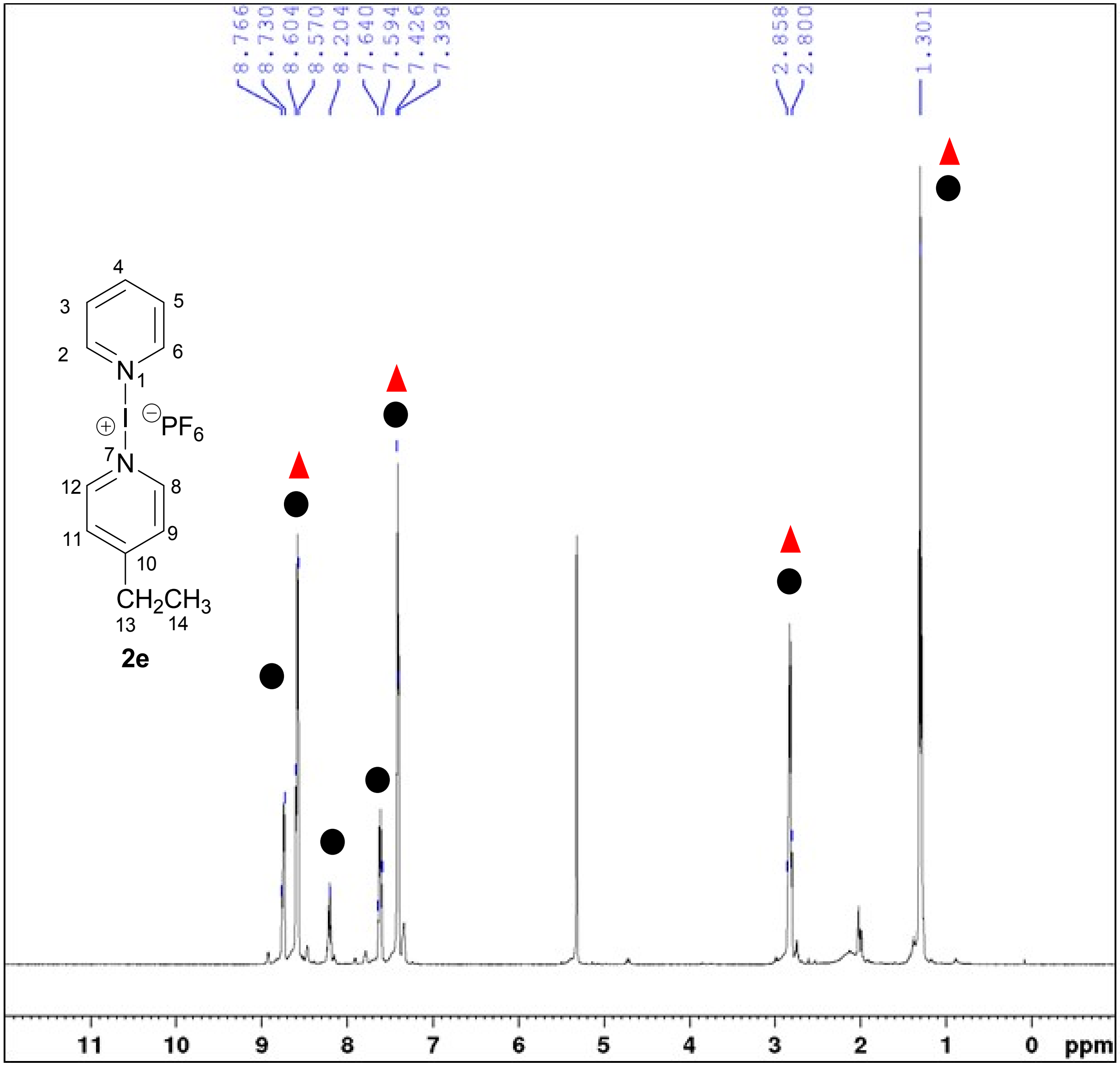

Figure S13. The ^{1}H NMR spectra of [I(py)(4-Etpy)]PF$_6$ (2e) (Colour Key: red triangle = 2d, black circle = 2e).

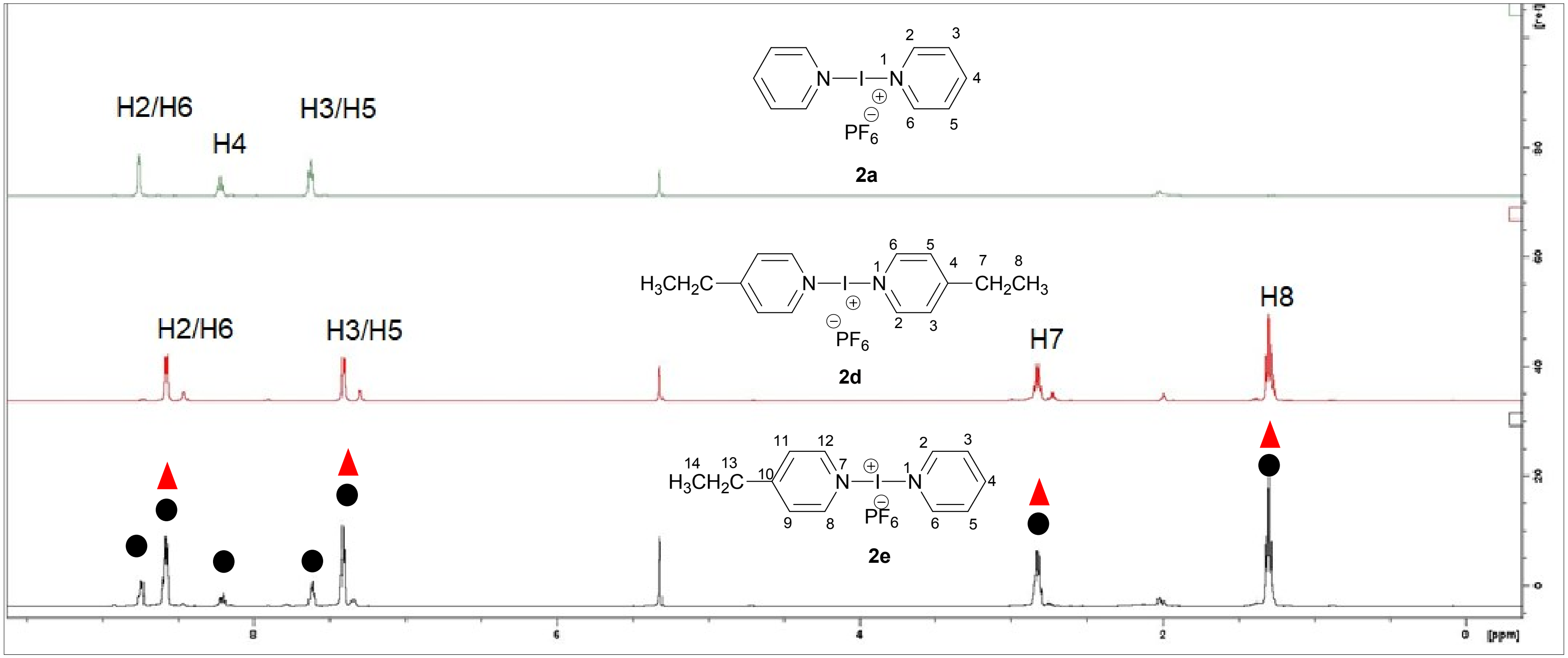

Figure S14. The compared ^{1}H NMR spectra of 2a, 2d and 2e (in CD_2Cl_2) (Colour Key: red triangle = 2d, black circle = 2e).

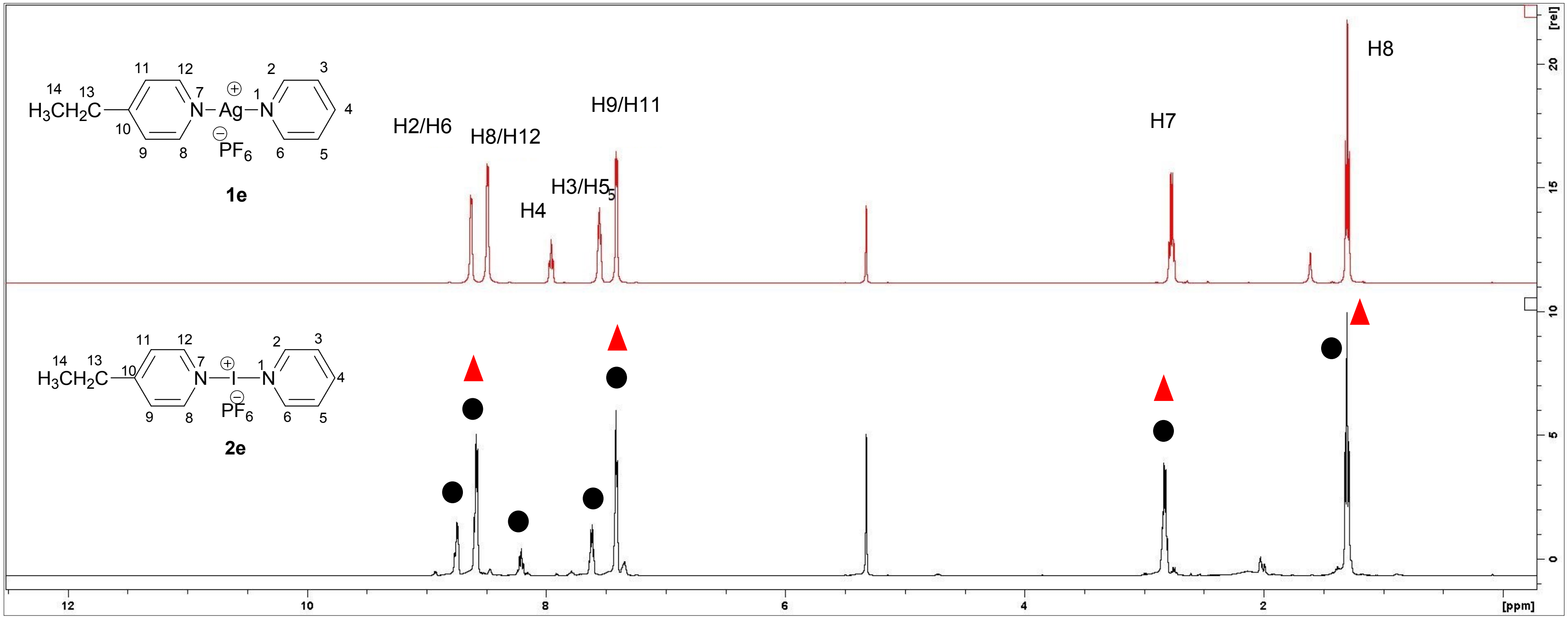

Figure S15. The compared ^{1}H NMR spectra of 1e and 2e (in CD_2Cl_2) (Colour Key: red triangle = 2d, black circle = 2e).

2.2 ^{1}H-^{15}N NMR Correlation spectra

Uncomplexed Ligands	**^{1}H-^{15}N δ values**
pyridine	-67.7 ppm
DMAP	-328.7 ppm, -108,9 ppm
4-ethylpyridine	-75.6

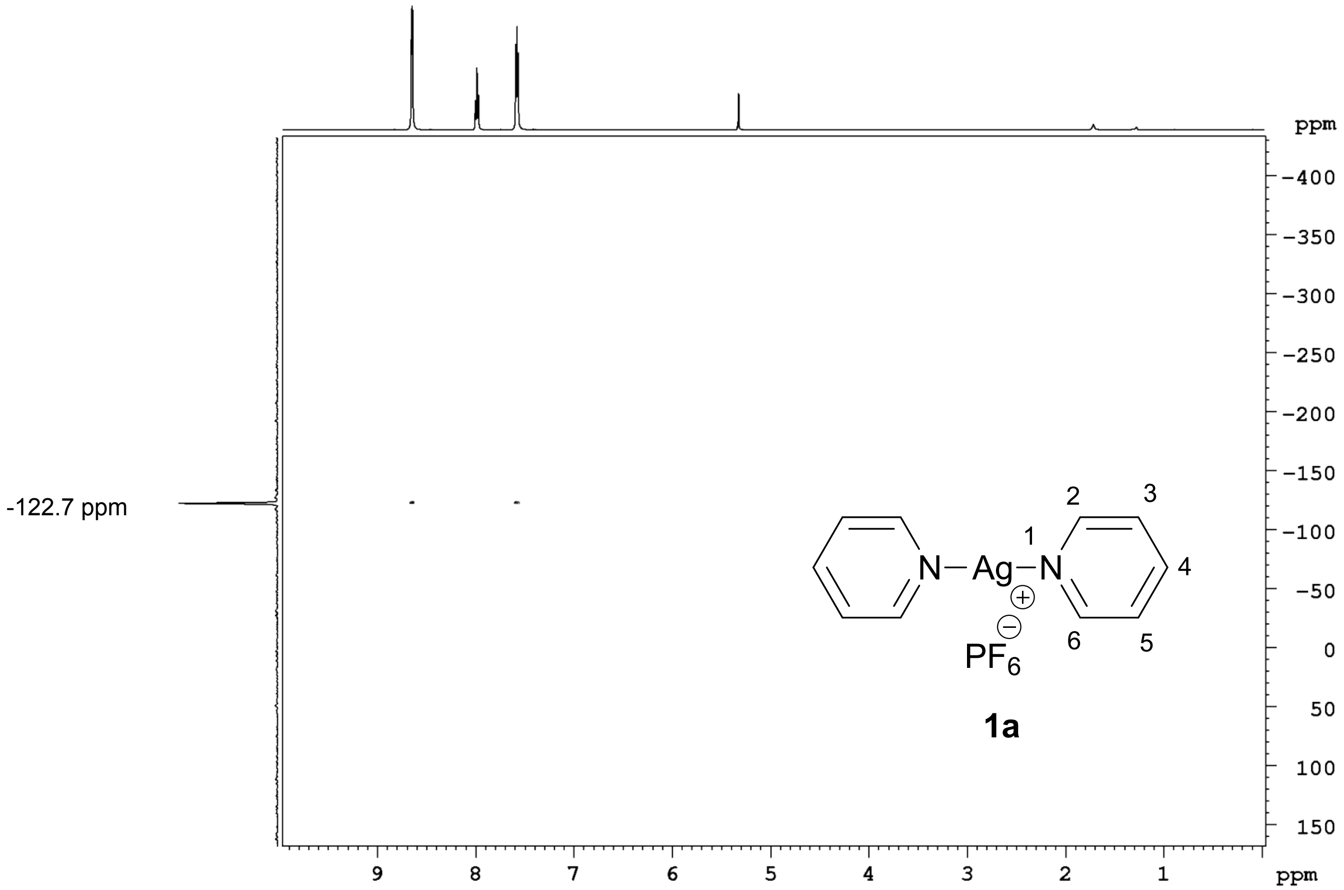

Figure S16. The ^{1}H-^{15}N NMR correlation spectra of 1a (in CD_2Cl_2).

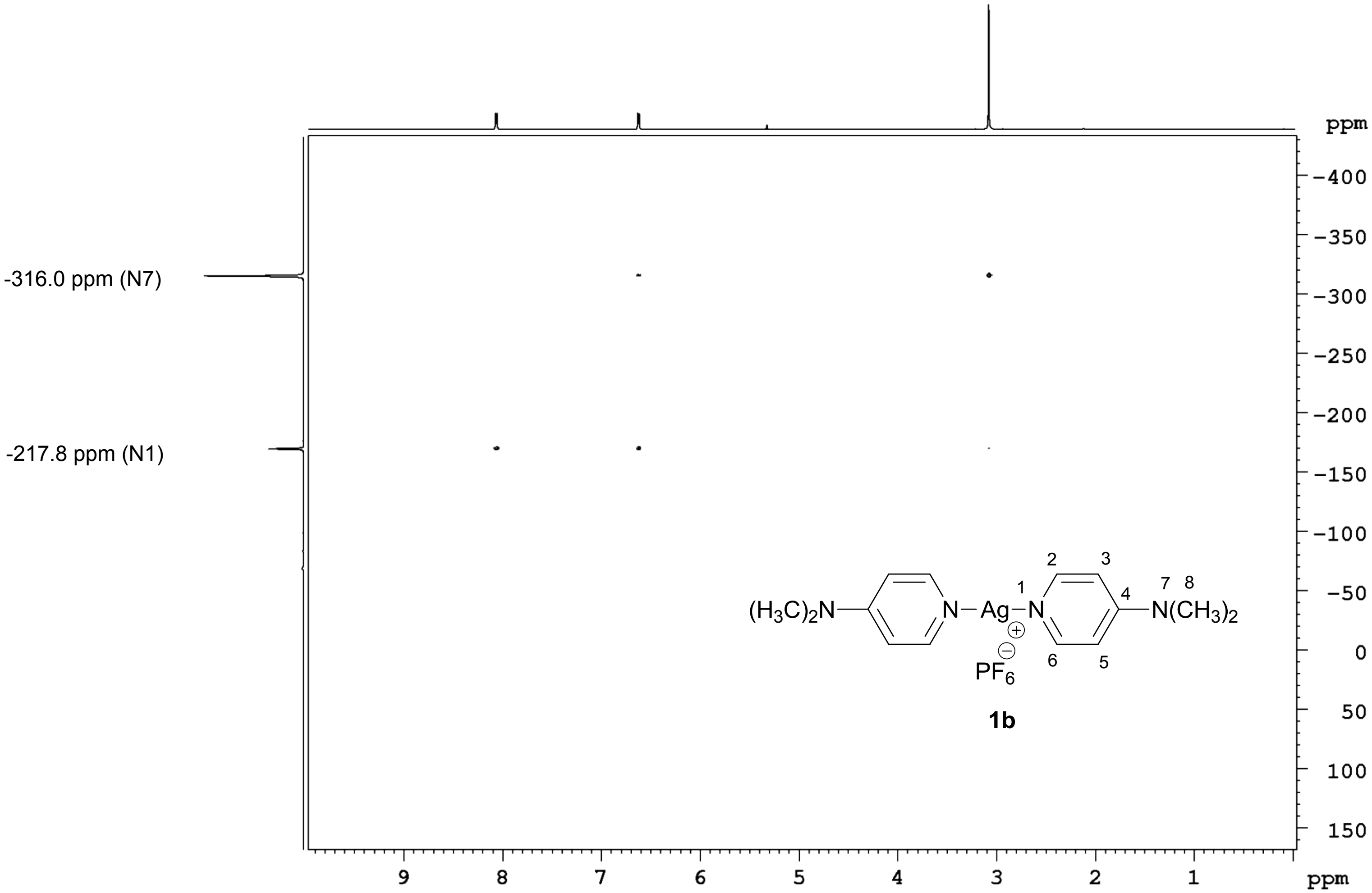

Figure S17. The ^{1}H-^{15}N NMR correlation spectra of 1b (in CD_2Cl_2).

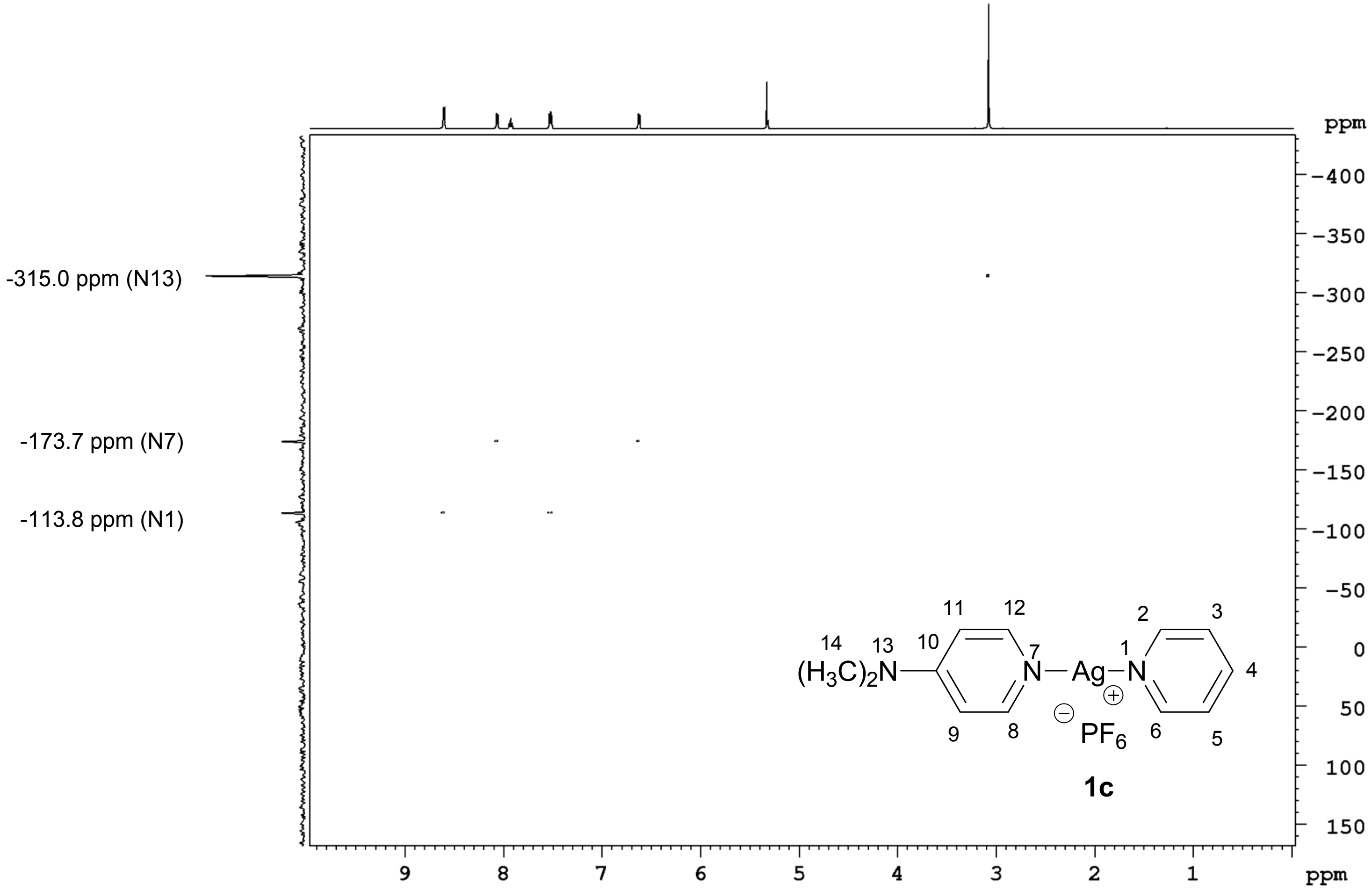

Figure S18. The ^{1}H-^{15}N NMR correlation spectra of 1c (in CD_2Cl_2).

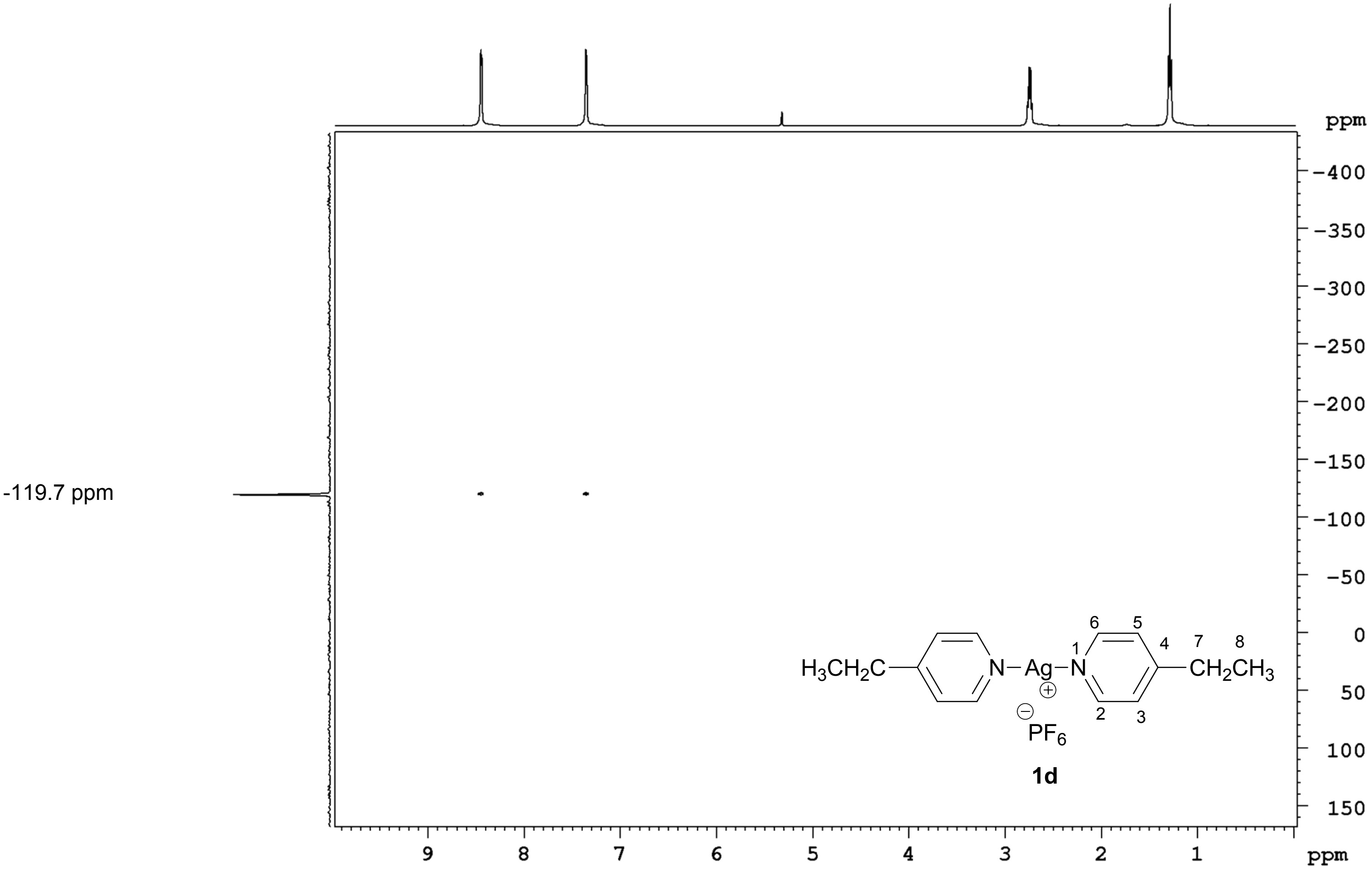

Figure S19. The ^{1}H-^{15}N NMR correlation spectra of 1d (in CD_2Cl_2).

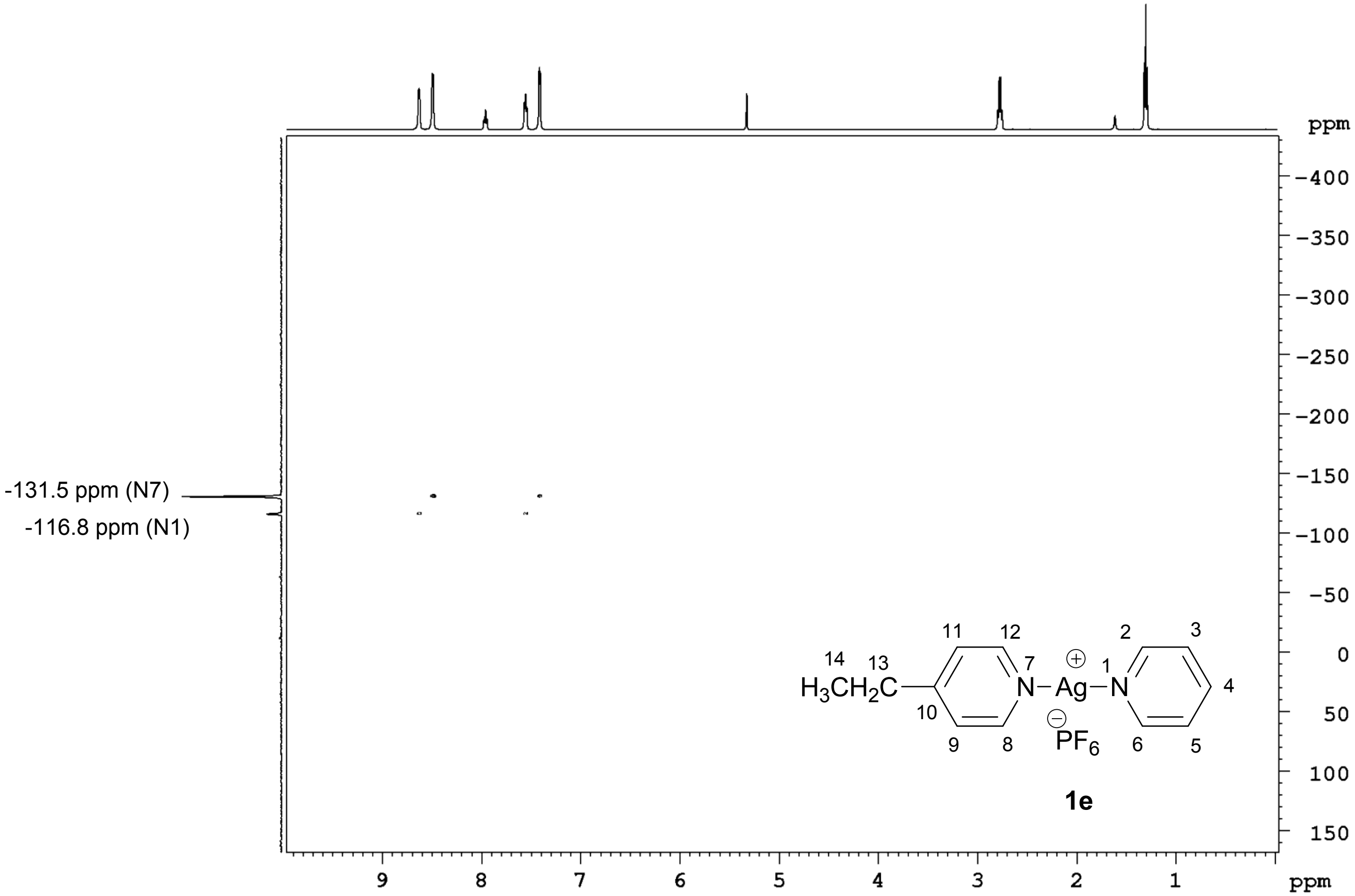

Figure S20. The ^1H-^{15}N NMR correlation spectra of 1e (in CD_2Cl_2).

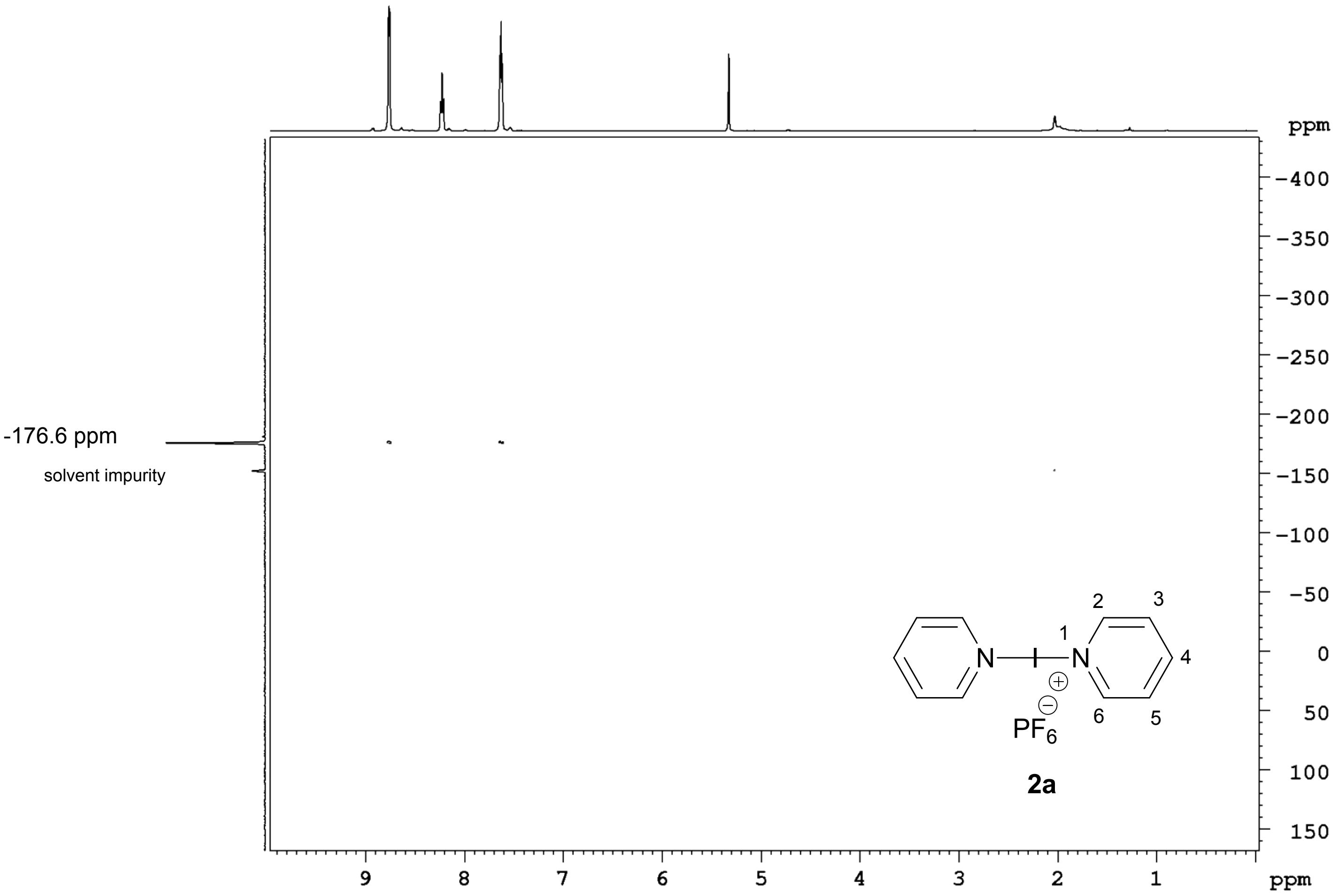

Figure S21. The ^{1}H-^{15}N NMR correlation spectra of 2a (in CD_2Cl_2).

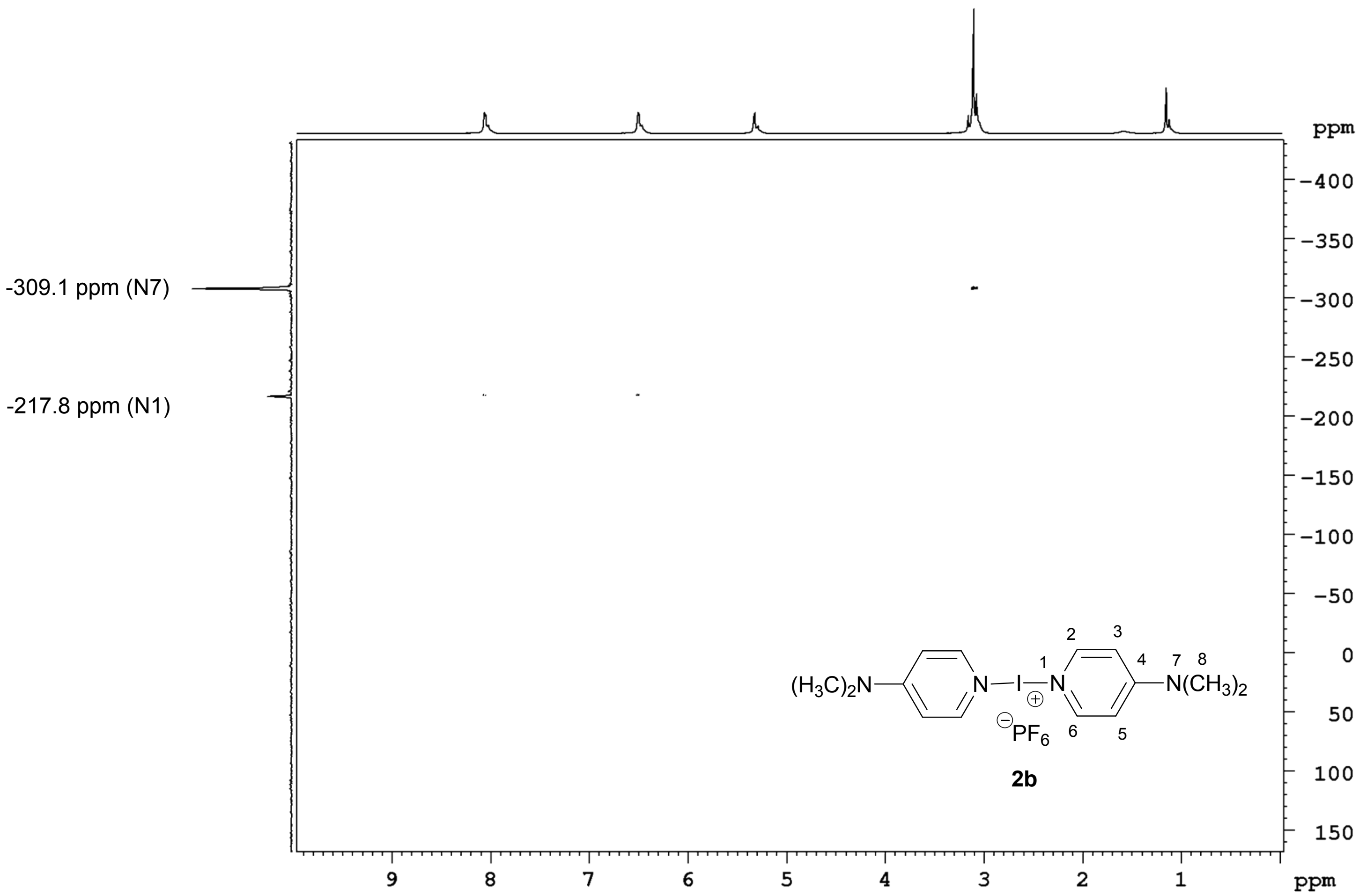

Figure S22. The ^{1}H-^{15}N NMR correlation spectra of 2b (in CD$_2$Cl$_2$).

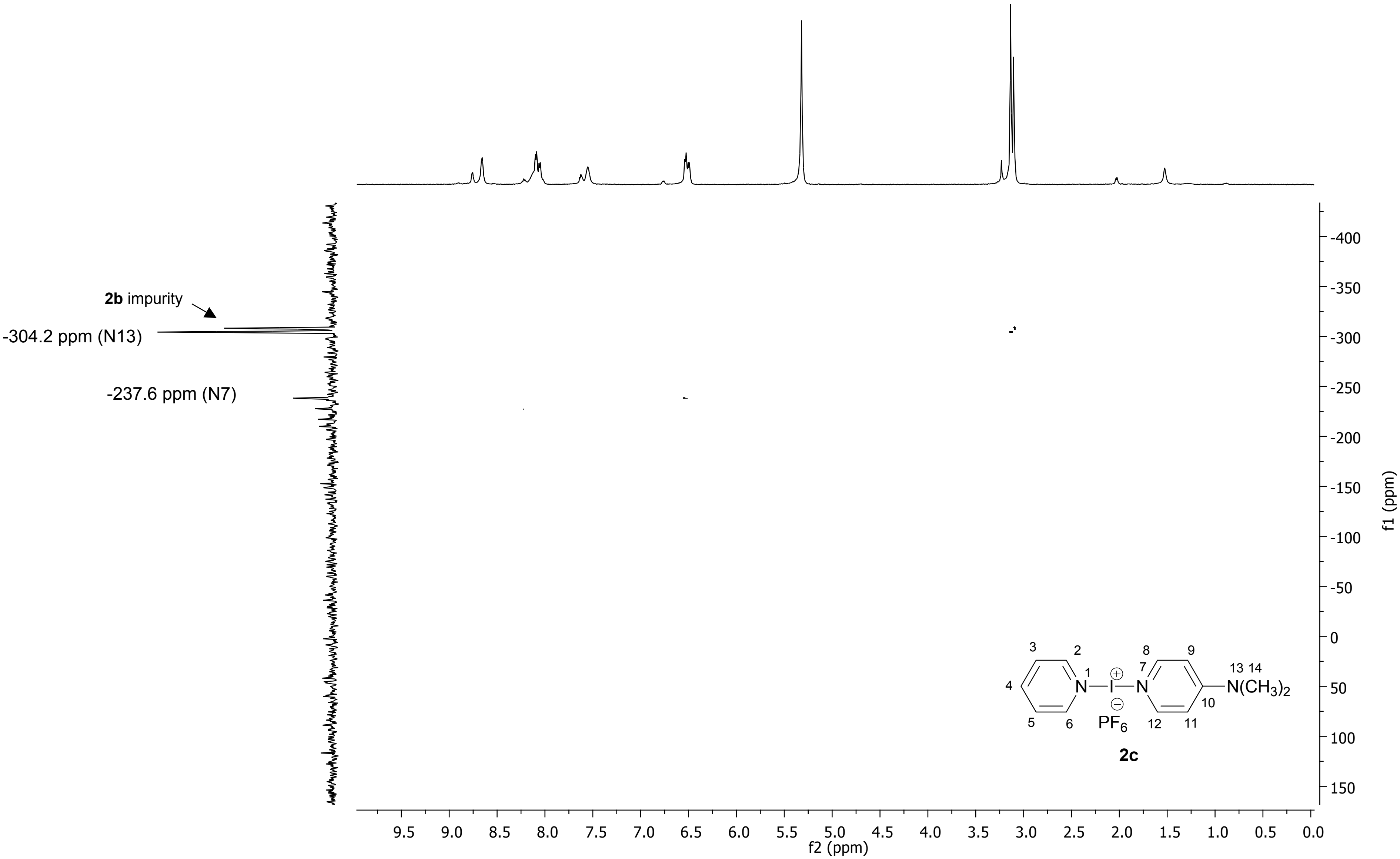

Figure S23. The ^1H-^{15}N NMR correlation spectra of 2c (in CD_2Cl_2).

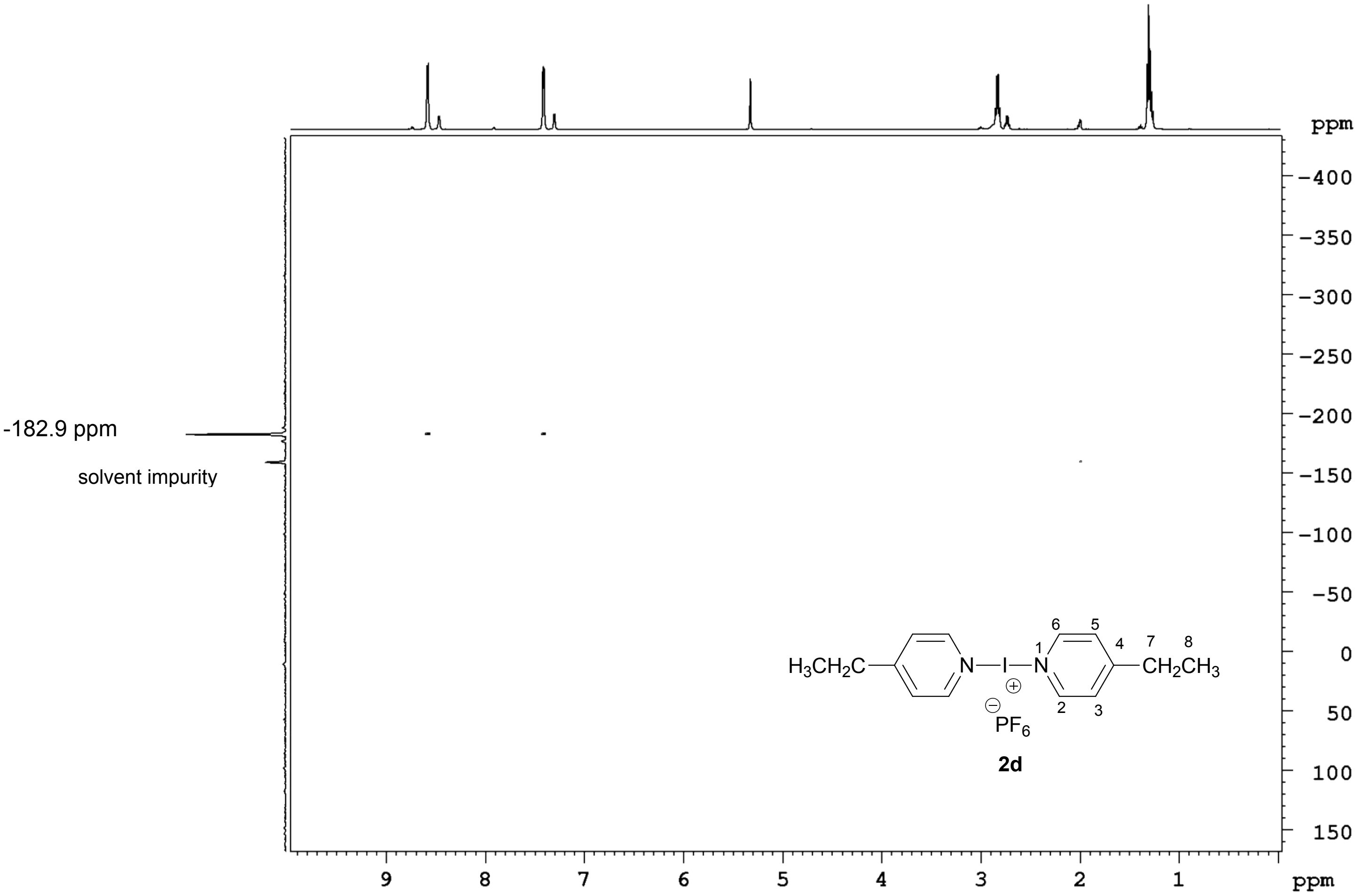

Figure S24. The ^{1}H-^{15}N NMR correlation spectra of 2d (in CD_2Cl_2).

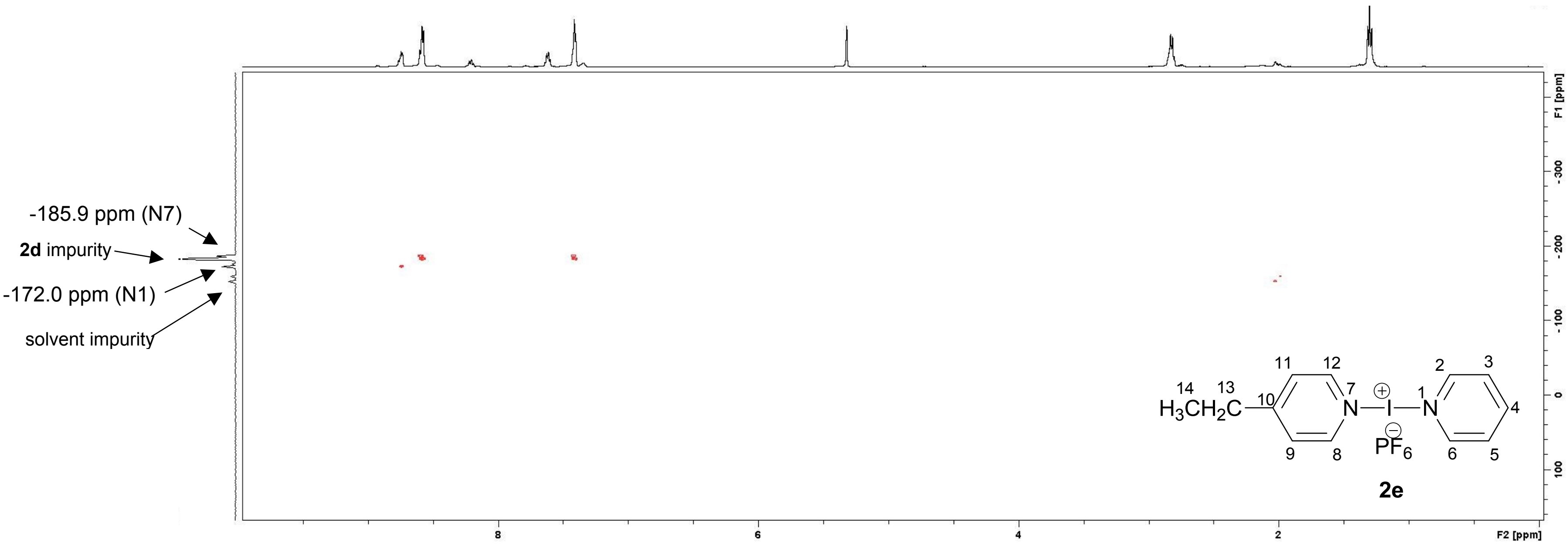

-185.9 ppm (N7)

2d impurity

-172.0 ppm (N1)

solvent impurity

Figure S25. The ^1H-^{15}N NMR correlation spectra of 2e (in CD_2Cl_2).

3. X-Ray Crystallography

The single crystal X-ray data for **1b_1**, **1c**, **1d**, and **1e** were collected at 170 K using Bruker-Nonius Kappa CCD diffractometer with an APEX-II detector with graphite-monochromatised Mo-Kα (λ = 0.71073 Å) radiation. Program COLLECT[3] was used for the data collection and DENZO/SCALEPACK[4] for the reduction. The single crystal X-ray data for **1b_2**, **1b_3**, and **2b** were collected at 120 K using an Agilent Super-Nova diffractometer with an Eos detector using mirror monochromated Mo-Kα (λ = 0.71073 Å) radiation. The single crystal X-ray data for **2c** was collected at 120 K using an Agilent Super-Nova dual wavelength diffractometer with an Atlas detector using mirror-monochromated Cu-Kα (λ = 1.54184 Å) radiation. The program CrysAlisPro[5] was used for the data collection and reduction on both Super-Nova diffractometers. The intensities were corrected for absorption using a gaussian face index absorption correction method.[5] The structures were solved by intrinsic phasing (SHELXT)[6] and refined by full-matrix least squares on F^2 using the OLEX2,[7] which utilises the SHELXL-2015 module.[8] Anisotropic displacement parameters were assigned to non-H atoms and isotropic displacement parameters for all H atoms were constrained to multiples of the equivalent displacement parameters of their parent atoms with $U_{iso}(H) = 1.2\ U_{eq}$ (parent atom). The X-ray single crystal data and CCDC numbers are given below.

1b_1

$[C_{14}H_{20}AgN_4][PF_6]\cdot C_7H_8$ (M = 589.31 gmol^{-1}): triclinic, space group *P*-1 (No. 2), *a* = 10.4171/6) Å, *b* = 10.7634(5) Å, *c* = 11.4213(7) Å, α= 100.440(4)º, *β* = 108.085(3)º, γ= 94.085(4)º, *V* = 1185.99(12) Å^3, *Z* = 2, T = 120 K, *μ*(Mo-Kα) = 0.98 mm^{-1}, D$_{calc}$ = 1.650 gcm^{-3}, 13360 reflections measured (1.9° ⩽ 2θ ⩽ 27.1°), 5174 unique (R$_{int}$ = 0.034) which were used in all calculations. The final refinement gave R$_1$ = 0.043 (I > 2σ(I)), *w*R$_2$ = 0.100, and *S* = 1.04. CCDC-1996937.

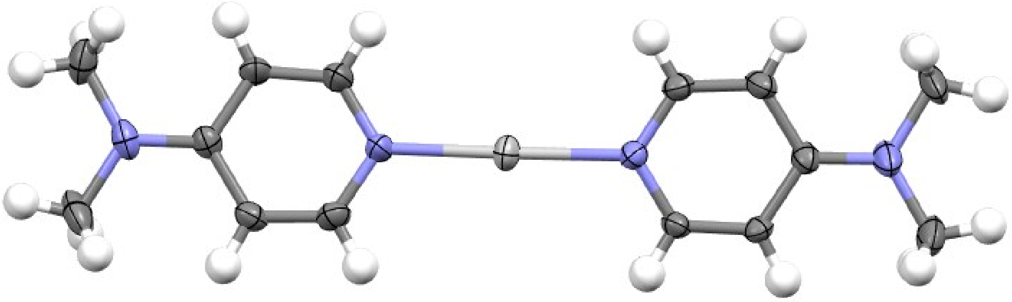

Figure S26. Crystal structure of 1b_1 (Thermal ellipsoids at 50% probability; hexafluorophosphate anion and solvates omitted for clarity; Colour Key: grey= silver, blue = nitrogen, dark grey = carbon).

1b_2

$[C_{14}H_{20}AgN_4][PF_6]$ (M = 497.18 gmol^{-1}): triclinic, space group *P*-1 (No. 2), *a* = 8.6651(13) Å, *b* = 10.6439(13) Å, *c* = 11.5780(16) Å, α= 90.059(7)º, *β* = 107.599(3)º, γ= 113.062(7)º, *V* = 918.0(2) Å^3, *Z* = 2, T = 170 K, *μ*(Mo-Kα) = 1.25 mm^{-1}, D$_{calc}$ = 1.799 gcm^{-3}, 5083 reflections measured (2.1° ⩽ 2θ ⩽ 26.4°), 3723 unique (R$_{int}$ = 0.033) which were used in all calculations. The final refinement gave R$_1$ = 0.063 (I > 2σ(I)), *w*R$_2$ = 0.139, and *S* = 1.05. CCDC-1996938.

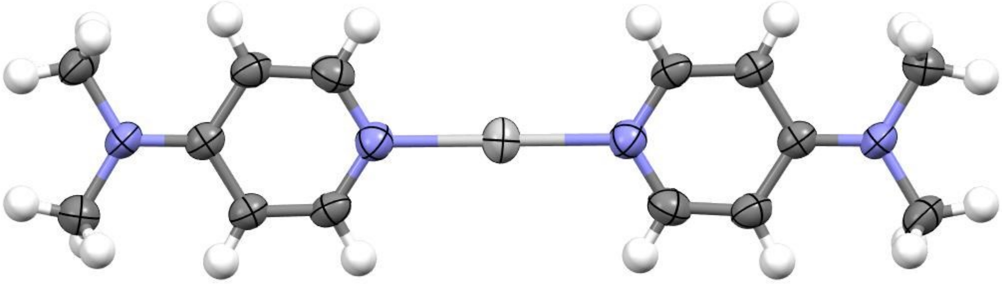

Figure S27. Crystal structure of 1b_2 (Thermal ellipsoids at 50% probability; hexafluorophosphate anion omitted for clarity; Colour Key: grey = silver, blue = nitrogen, dark grey = carbon).

1b_3

$[C_{14}H_{20}AgN_4][PF_6]\cdot C_2H_4Cl_2$ (M = 596.13 gmol^{-1}): triclinic, space group *P*-1 (No. 2), *a* = 7.7214(6) Å, *b* = 10.5840(8) Å, *c* = 14.3078(15) Å, α= 109.040(8)º, *β* = 90.185(7)º, γ= 90.561(7)º, *V* = 1105.23(17) Å^3, *Z* = 2, T = 120 K, *μ*(Mo-Kα) = 1.29 mm^{-1}, D$_{calc}$ = 1.791 gcm^{-3}, 15571 reflections measured (2.0° ⩽ 2θ ⩽ 27.1°), 4822 unique (R$_{int}$ = 0.048) which were used in all calculations. The final refinement gave R$_1$ = 0.073 (I > 2σ(I)), *w*R$_2$ = 0.208, and *S* = 1.03. CCDC-1996939.

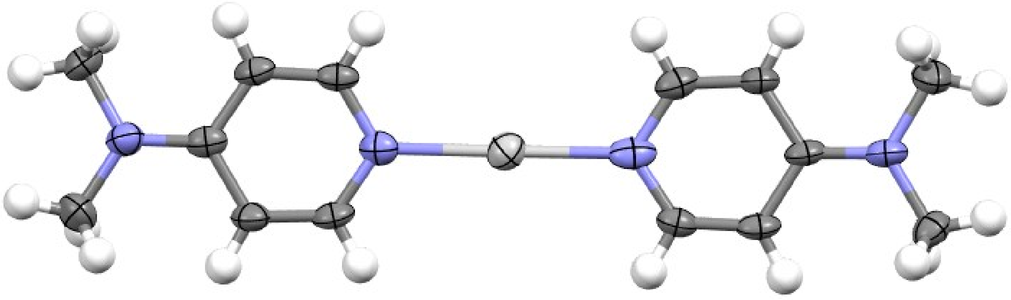

Figure S28. Crystal structure of 1b_3 (Thermal ellipsoids at 50% probability; hexafluorophosphate anion and solvates omitted for clarity; Colour Key: grey= silver, blue = nitrogen, dark grey = carbon).

1c

$[C_{12}H_{15}AgN_3][PF_6]$ (M = 454.11 gmol^{-1}): monoclinic, space group $P2_1/n$, a = 7.8394(5) Å, b = 14.2529(8) Å, c = 14.6397(8) Å, β = 100.629(3)º, V = 1607.69(16) Å^3, Z = 4, T = 170 K, μ(Mo-Kα) = 1.41 mm^{-1}, D_{calc} = 1.876 gcm^{-3}, 5158 reflections measured ($2.8° \leqslant 2\theta \leqslant 25.7°$), 2894 unique ($R_{int}$ = 0.046) which were used in all calculations. The final refinement gave R_1 = 0.091($I > 2\sigma(I)$), wR_2 = 0.202, and S = 1.14. CCDC-1996940.

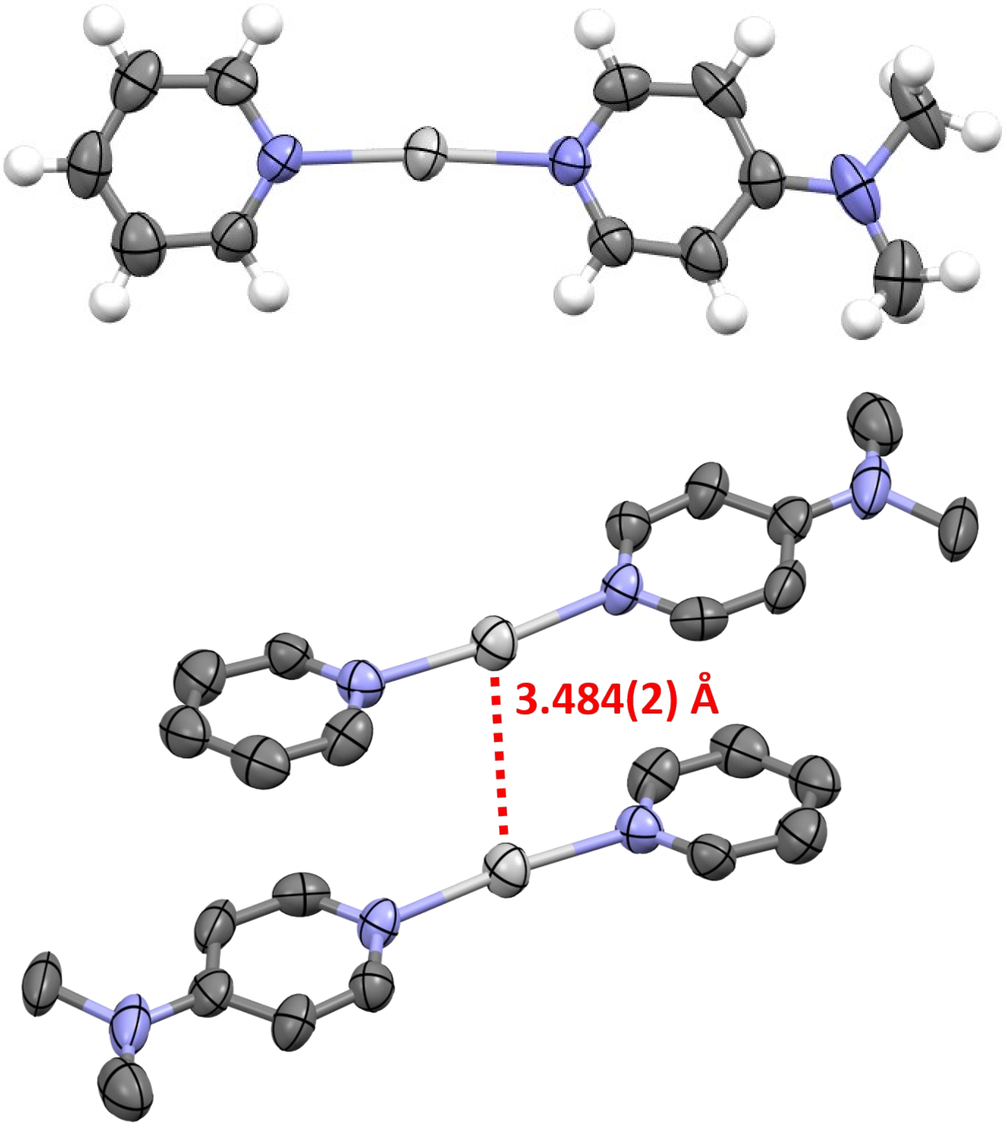

Figure S29. The crystal structure of 1c (top) and the dimeric $Ag^+\cdots Ag^+$ interaction between two molecules of 1c (bottom; hydrogen atom omitted for clarity). (Thermal ellipsoids at 50% probability; hexafluorophosphate anions omitted for clarity; Colour Key: grey = silver, blue = nitrogen, dark grey = carbon).

1d

[$C_{14}H_{18}AgN_2$][PF_6] (M = 467.14 gmol^{-1}): monoclinic, space group $P2_1/n$, a = 8.0602(2) Å, b = 19.5517(3) Å, c = 10.8483(2) Å, β = 90.690(7)º, V = 1709.47(6) Å^3, Z = 4, T = 170 K, μ(Mo-Kα) = 1.33 mm^{-1}, D$_{calc}$ = 1.815 gcm^{-3}, 14940 reflections measured (2.7° $\leqslant 2\theta \leqslant$ 27.1°), 3747 unique (R$_{int}$ = 0.026) which were used in all calculations. The final refinement gave R$_1$ = 0.028 (I > 2σ(I)), wR$_2$ = 0.066, and S = 1.03. CCDC-1996941.

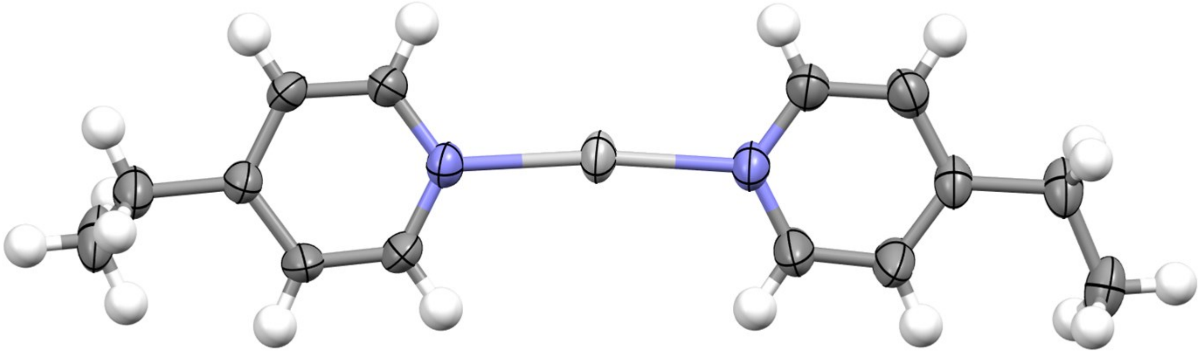

Figure S30. The crystal structure of 1d (Thermal ellipsoids at 50% probability; disorder and hexafluorophosphate omitted for clarity; Colour Key: grey = silver, blue = nitrogen, dark grey = carbon).

1e

$[C_{12}H_{14}AgN_2][PF_6]$ (M = 439.09 $gmol^{-1}$): triclinic, space group *P*-1 (No. 2), *a* = 8.4968(8) Å, *b* = 9.1809(11) Å, *c* = 10.9655(14) Å, *α* = 72.296(5)º, *β* = 71.948(7)º, *γ* = 73.418(7)º, *V* = 757.33(16) $Å^3$, *Z* = 2, T = 170 K, *μ*(Mo-Kα) = 1.50 mm^{-1}, D_{calc} = 1.926 gcm^{-3}, 6348 reflections measured ($2.6° \leqslant 2\theta \leqslant 27.1°$), 3300 unique ($R_{int}$ = 0.048) which were used in all calculations. The final refinement gave R_1 = 0.063 (I > 2σ(I)), wR_2 = 0.163, and *S* = 1.03. CCDC-1996942.

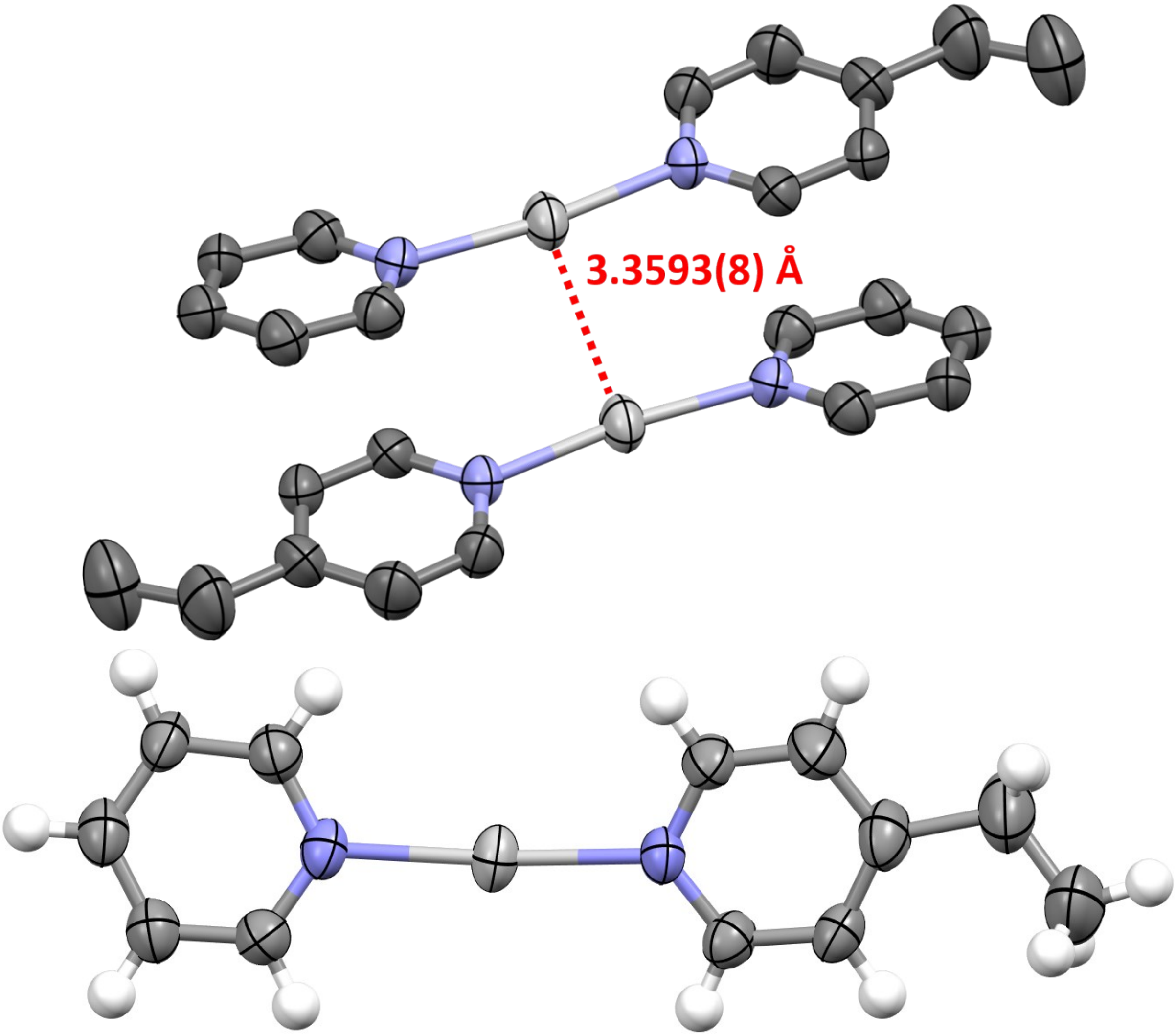

Figure S31. The crystal structure of 1e (top) and the dimeric Ag$^+$···Ag$^+$ interaction between two molcules of 1e (bottom; hydrogen atom omitted for clarity). (Thermal ellipsoids at 50% probability; hexafluorophosphate anions omitted for clarity; Colour Key: grey = silver, blue = nitrogen, dark grey = carbon).

2b

$[C_{14}H_{20}IN_4][PF_6]\cdot CH_2Cl_2$ (M = 601.13 gmol^{-1}): monoclinic, space group $P2_1/m$, a = 9.9904(3) Å, b = 10.3032(2) Å, c = 11.8320(4) Å, β = 114.588(4)º, V = 1107.47(6) Å^3, Z = 2, T = 120 K, μ(Mo-Kα) = 1.82 mm^{-1}, D_{calc} = 1.803 gcm^{-3}, 5002 reflections measured (1.9° ⩽ 2θ ⩽ 28.3°), 6611 unique (R_{int} = 0.028) which were used in all calculations. The final refinement gave R_1 = 0.031 ($I > 2\sigma(I)$), wR_2 = 0.070, and S = 1.04. CCDC-1996943.

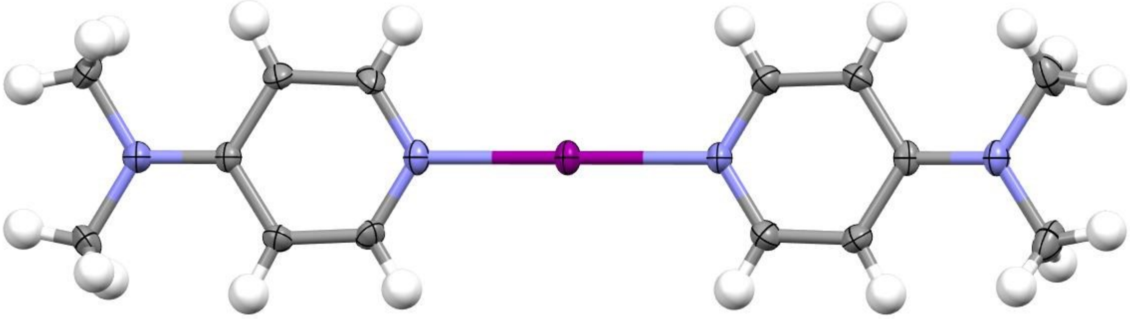

Figure S32. Crystal structure of 2b (Thermal ellipsoids at 50% probability; hexafluorophosphate anion and solvates omitted for clarity; Colour Key: purple= iodine, blue = nitrogen, grey = carbon).

2c.

$[C_{12}H_{15}IN_3][PF_6]\cdot0.5(CH_2Cl_2)$ (M = 515.60 gmol^{-1}): monoclinic, space group $C2/m$ a = 22.793(3) Å, b = 10.3913(9) Å, c = 8.4476(5) Å, β = 91.168(8)º, V = 2000.4(3) Å^3, Z = 4, T = 120 K, μ(Cu-Kα) = 15.09 mm^{-1}, D_{calc} = 1.712 gcm^{-3}, 7587 reflections measured (3.9° $\leqslant 2\theta \leqslant$ 74.5°), 2152 unique (R_{int} = 0.073) which were used in all calculations. The final refinement gave R_1 = 0.102 ($I > 2\sigma(I)$), wR_2 = 0.295, and S = 1.25. CCDC-1996944.

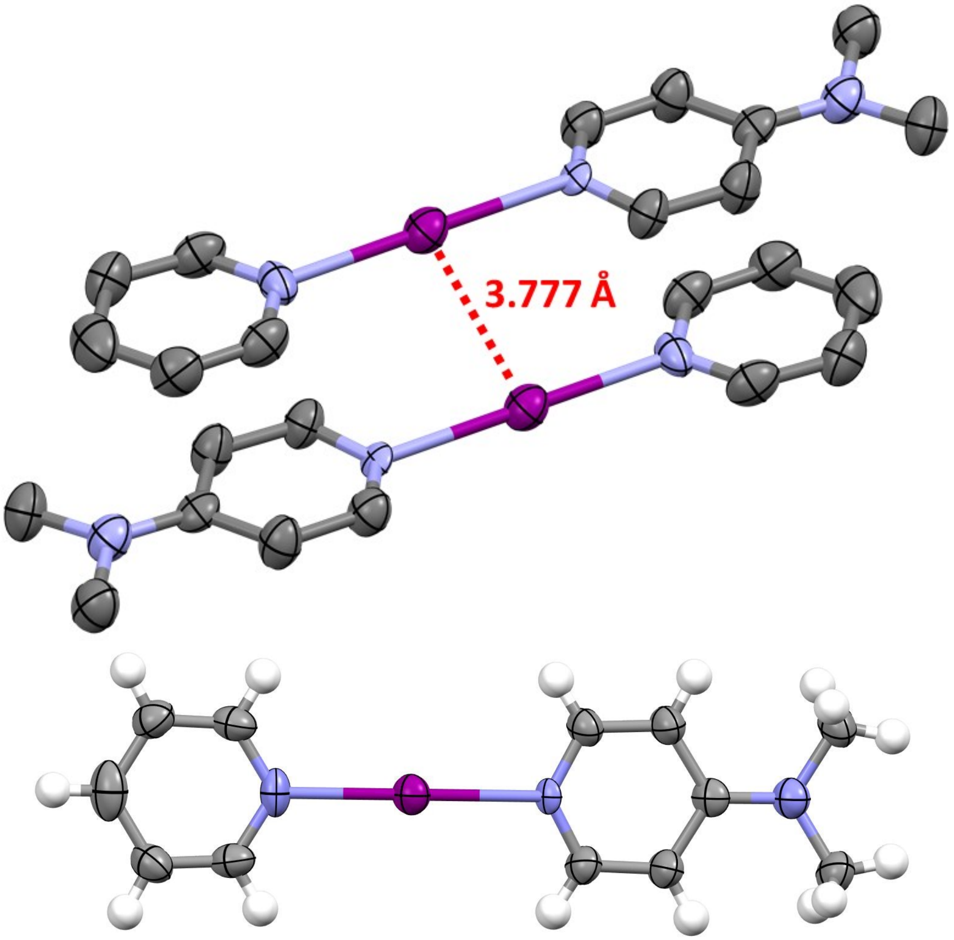

Figure S33. Crystal structure of 2c (top) and the dimeric $I^+\cdots I^+$ close contact between two molcules of 2c (bottom; hydrogen atom omitted for clarity). (Thermal ellipsoids at 50% probability; hexafluorophosphate anion and solvates omitted for clarity; Colour Key: purple= iodine, blue = nitrogen, grey = carbon).

4. Theoretical methods

For the calculations we have used the M06-2X functional[9] combined with the def2-TZVP basis set[10] as implemented in the Gaussian-16 program.[11] For the analysis of the asymmetric distances and orbitals (see below), the geometries have been fully optimized and they correspond to true minima apart from those where the planarity has been imposed for comparison). The X-ray coordinates have been used for the analysis of the interactions in the X-ray dimers. The NBO,[12] AIM[13] and NCIplot calculations[14] have been computed using the same level of theory. The AIM analysis has been performed using the AIMAll program.[15]

4.1 DFT study

This study is devoted to compare the argentophillic Ag(+)···Ag(+) interactions observed in the X-ray crystal structures of complexes **1b-e** (see Figure **S34**) to the I(+)···I(+) interaction in compound **2c**. For this study we have used DFT calculations combined with the quantum theory of atoms-in-molecules (QTAIM) analysis, noncovalent interaction plot (NCIplot) and natural bond orbital (NBO) computational tools. Remarkably, these compounds have a strong tendency to form discrete dimers in the solid state where in addition to the π-stacking interactions between the aromatic ligands, the Ag(I) metal centers interact with Ag···Ag distances ranging from 3.31 to 3.48 Å that are similar to the sum of their Van der Waals radii (3.44 Å, see Figure **S34**).

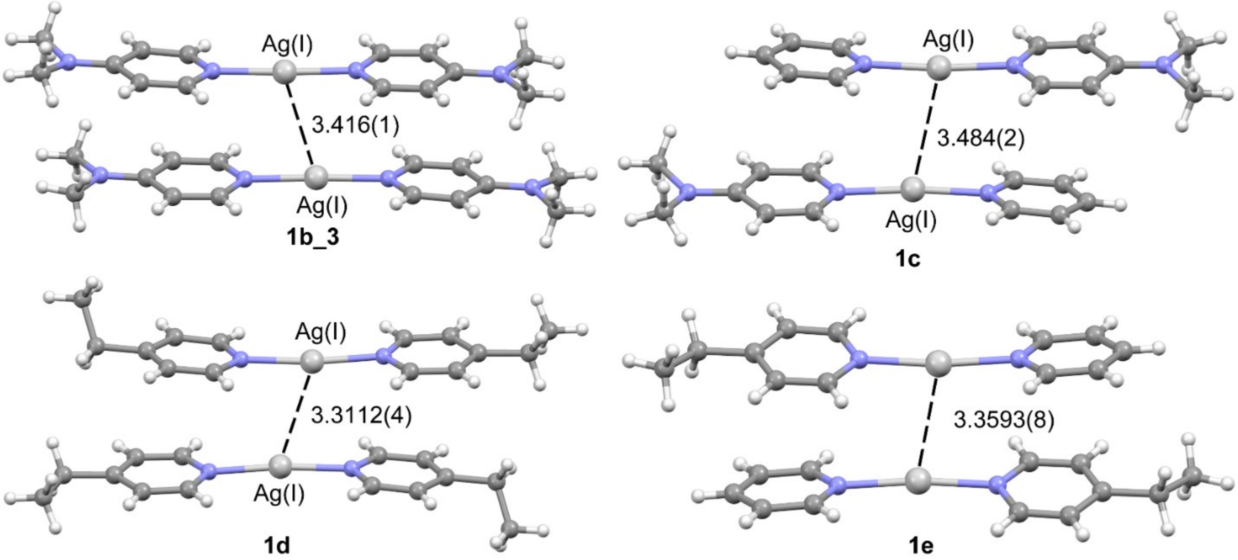

Figure S34. Self-assembled dimers observed in the solid state of compounds 1b-e (distances in Å).

Regarding the complexes where the Ag(I) has been replaced by I(+), only compound **2c** exhibits the formation of similar dimers with short I···I contacts (sum of Van der Waals radii 3.96 Å). To our knowledge this type of interaction has not previously described in the literature.

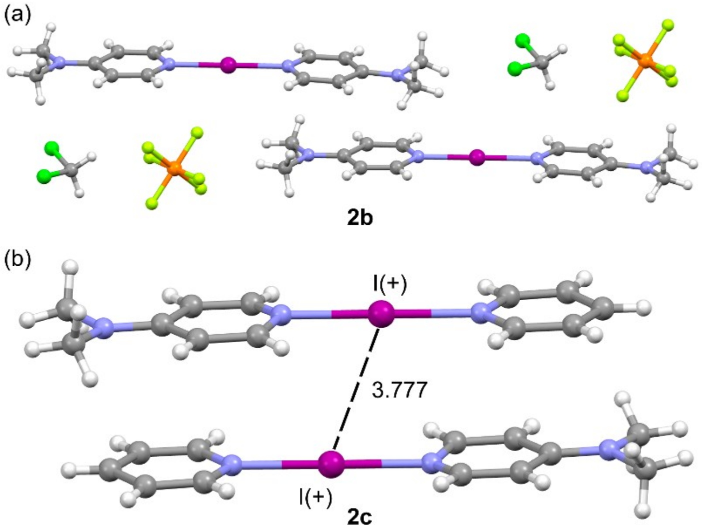

Figure S35. (a) Partial view of the X-ray solid state structure of 2b (b); Self-assembled dimer observed in the solid state of compound 2c (distances in Å).

First, we have performed the QTAIM analysis of the dimers shown in Figure **S34**. The existence of a bond critical point and bond path interconnecting to atoms is considered an unambiguous evidence of interaction.[16] The distributions of bond critical points (BCPs) and bond paths for all dimers are given in Figure **S36**. For clarity, ring and cage CP are not shown in the representation. For all dimers of compounds **1b-e** (Figure **2a**), the distribution shows the presence of a BCP (green sphere) and bond path interconnecting the Ag atoms and confirming the existence of the argentophilic interaction. In addition, several BCPs and bond paths interconnect several C/N-atoms of the ligands thus characterising the π–π stacking interactions. In compound **1b_3** the distribution of CPs and bond paths also reveals the existence of C–H···N H-bonds between methyl and N-atom of the amino groups. In compound **2c** the I(+)···I(+) contact is characterised by a BCP and bond path interconnecting both I atoms, thus confirming the existence of the interaction.

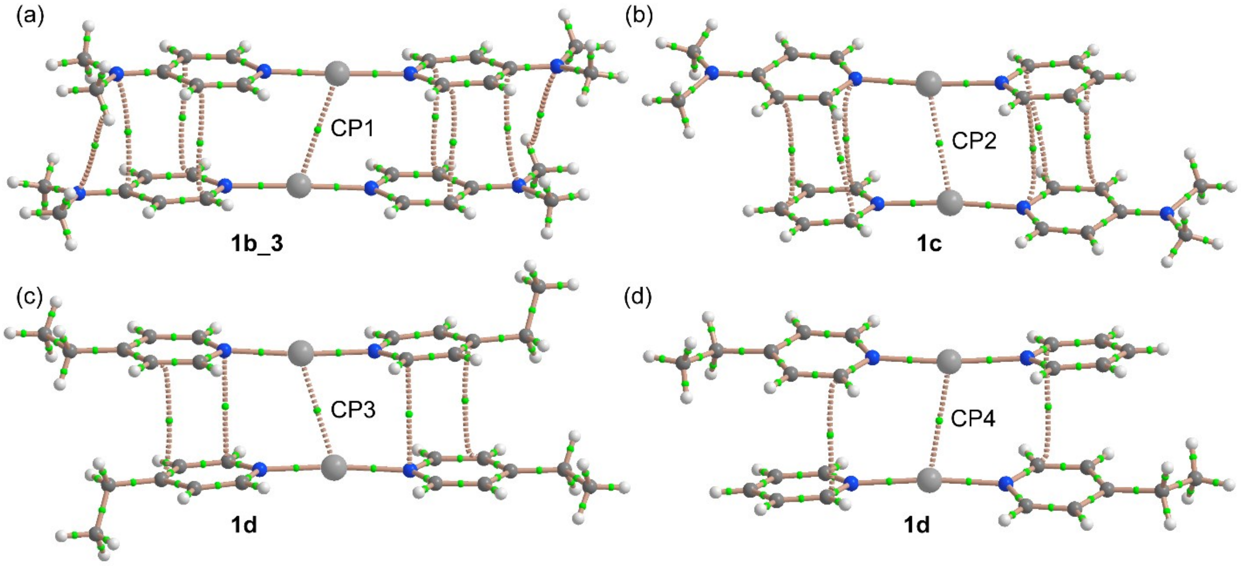

Figure S36. Distribution of bond critical points (green spheres) and bond paths (dashed ones correspond to noncovalent interactions) for the dimers of compounds 1b–1e.

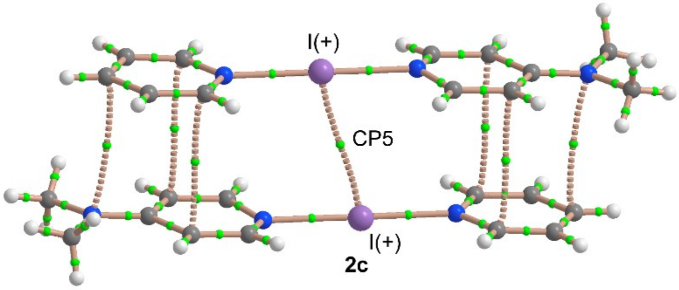

Figure S37. Distribution of bond critical points (green spheres) and bond paths (dashed ones correspond to noncovalent interactions) for the dimer of compound 2c.

Table **S1** summarizes the values or density [ρ(r)], Laplacian [$\nabla^2\rho(r)$], kinetic energy density [V(r)], Lagrangian energy density [G(r)] and total energy density [H(r)] at the bond critical points that interconnect the Ag(+) or I(+) atoms. The positive values or the Laplacian combined with positive values of H(r) confirm the noncovalent nature of the interaction in all dimers.

Table S 1. QTAIM parameters (a.u.) at the critical points labelled in Figures S36 and S37

Name	**ρ(r)**	**$\nabla^2\rho(r)$**	**V(r)**	**G(r)**	**H(r)**
CP1	0.009681	+0.026022	-0.005661	+0.006083	+0.000422
CP2	0.008583	+0.022085	-0.004689	+0.005105	+0.000416
CP3	0.011383	+0.032176	-0.007473	+0.007758	+0.000285
CP4	0.010514	+0.028935	-0.006523	+0.006878	+0.000355
CP5	0.011609	+0.027783	-0.005894	+0.006420	+0.000526

We have also used the NCIplot index[14] to further analyse both argentophilic and I(+)···I(+) interactions. The NCI plot helps to identify and visualise non-covalent interactions. This index is based on the peaks that appear in the reduced density gradient (RDG) at low densities. The formation of a supramolecular complex induces a significant change in the RDG at the critical points in between the interacting molecules due to the annihilation of the density gradient at these points. Consequently, the NCI plot is useful to evaluate host–guest complementarity and the extent to which noncovalent forces stabilise a complex. The information is basically qualitative showing which molecular regions interact using a colour scheme (red-yellow-green-blue scale). Red and blue colours are used to represent repulsive (ρ^{+}_{cut}) and attractive (ρ^{-}_{cut}) interactions, respectively. The yellow and green colours are used to represent weak repulsive and weak attractive forces, respectively. The representations of the NCI plots of two representative dimers **1c** and **2c** are shown in Figure **S37**. In both dimers, the plot shows an extended and green isosurface that embraces both ligands and also includes the region between both Ag or I atoms. In the dimer of **2c**, the surface between both I(+) is slightly better defined than the isosurface between the Ag(+)···Ag(+) in **1c**. It is interesting to highlight that this analysis not only confirms the existence of the interactions but also suggests that both the argentophilic and the I(+)···I(+) interactions are attractive.

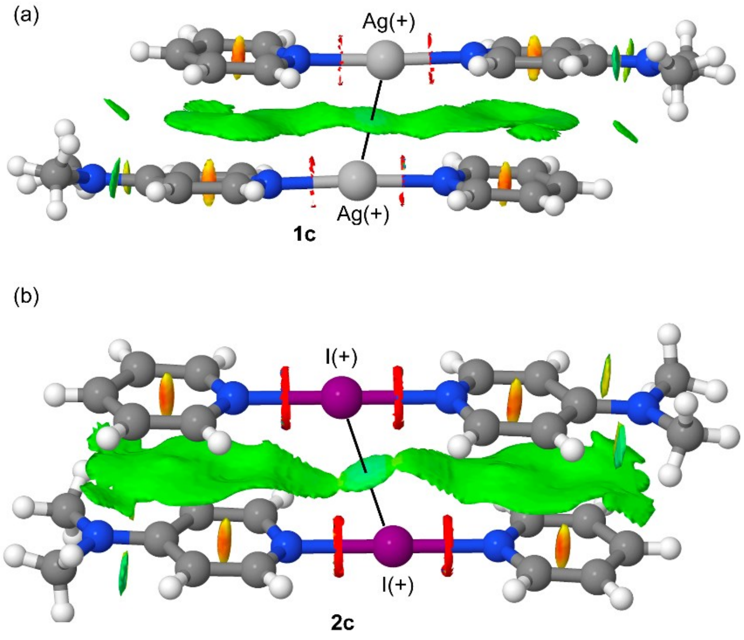

Figure S38. NCIplot of the dimers of 1c (a) 2c B (b). The gradient cut-off is *s* = 0.35 au, and the colour scale is −0.04 < ρ < 0.04 au.

The importance of orbital interactions has been studied using the dimers of **1c** and **2c**. The noncovalent forces described above occur against the Coulombic repulsion between two positively charged atoms. However, it is well known[17] that Ag(I) centres have a strong tendency to form "like-like" interactions with a wide range of distances: between the sum of Van der Waals radii and the distance of Ag–Ag single bond (2.53 Å). It has been proposed that orbital donor-acceptor contributions are important to explain the argentophilic interactions.[18] Therefore, we have used Natural Bond Orbital (NBO) calculations, focusing our attention on the second order perturbation analysis,[12] because it is adequate to investigate energy stabilisation associated to the donor–acceptor interactions.[12] For dimer **1c**, we have found a relevant orbital contribution (9.54 kcal/mol) due to an electron donation from a 4*d* atomic orbital of Ag(1) to the empty 5*s* orbital of Ag(2). Additionally, an equivalent "retro-donation" 4*d*(Ag2)→5*s*(Ag1) is also observed (see Figure **S39**). Consequently, the total donor–acceptor orbital stabilisation $E^{(2)}$= 19.08 kcal/mol which is similar to other calculations involving Ag dimers.[18,19] The NBO analysis in the **2c** dimer shows two modest orbital contributions; one corresponds to a donation from a lone pair (LP) orbital of I(1) to the 5*d* atomic orbital of I(2) with a concomitant stabilisation energy of 0.63 kcalmol^{-1} and another one that corresponds to a donation from the LP orbital of I(1) to a 6*p* atomic orbital of I(2) (0.33 kcalmol^{-1}). Additionally, an equivalent "retro-donation" LP{I(2)}→5*d*/6*p*{I(1)} is also observed (see Figure **S39**).The LP orbital is basically localised in a *p* atomic orbital of I. This analysis shows that whilst the argentophilic interaction is dominated by orbital effects, the I···I interaction has a small contribution from donor-acceptor interactions between the I-atoms. Therefore, the I(+)···I(+) contact is likely dominated by dispersion or polarisation effects. In the particular case of **2c**, π-stacking interactions and also the counterion likely have a major role in the formation of the dimer observed in the solid state of **2c**.

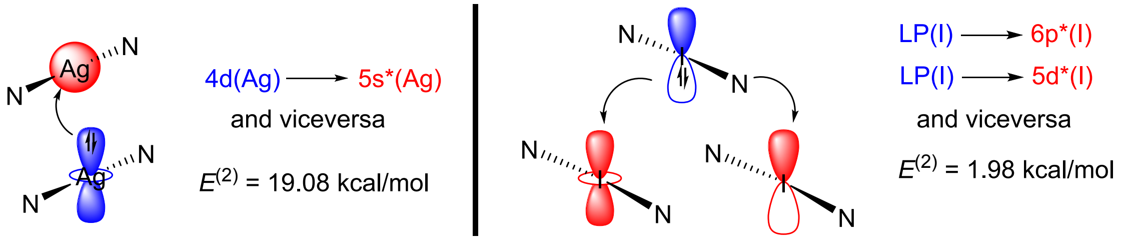

Figure S39. Representation of the orbital donor-acceptor interactions in dimers of A (left) and B (right).

We have fully optimized the symmetric and asymmetric complexes using pyridine and dmap as ligands. The optimized geometries of the symmetric complexes are shown in **Figure S40**. We have used two conformations for the complexes, rotated (global minima) and coplanar. For the latter only the coplanarity of the rings has been imposed and the rest of the molecule has been fully relaxed. This has been done to mimic the crystal packing, since the rings are coplanar in the X-ray structures. It can be observed that for the symmetric complexes both N–Ag,I distances are equivalent. In general, the experimental distances are shorter than the theoretical ones. The differences between the theoretical distances in the rotated and coplanar geometries are very small.

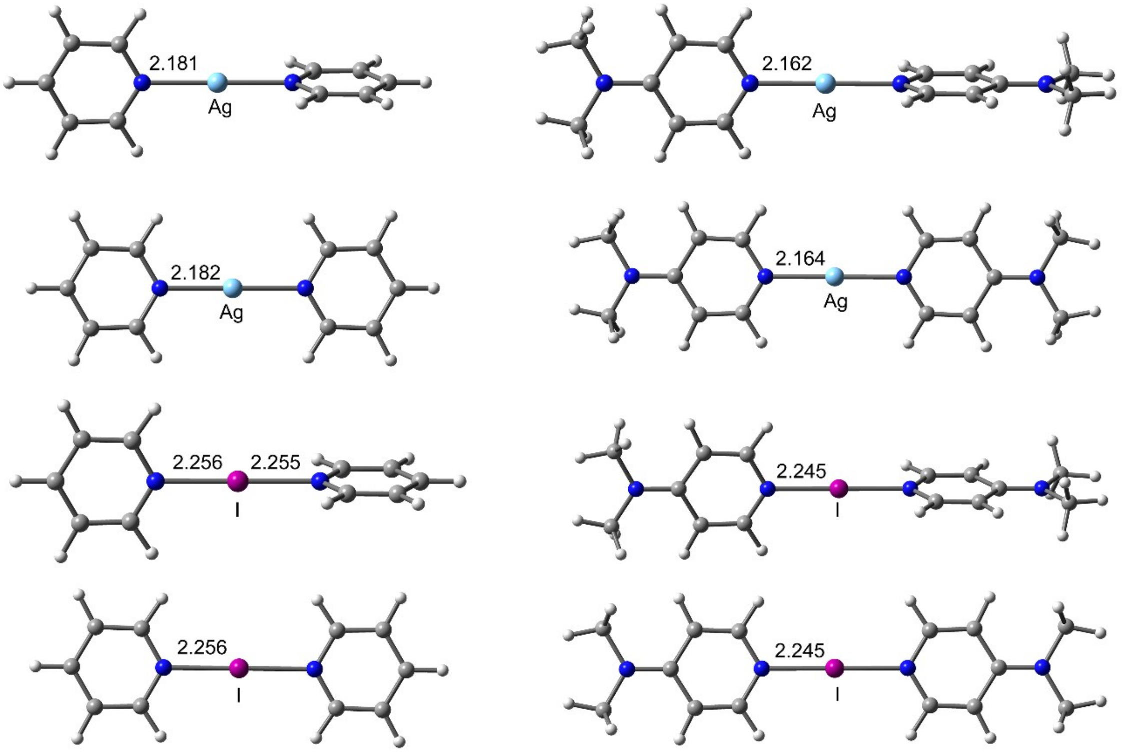

Figure S40. M06-2X/def2-TZVP optimized geometries of the symmetric compounds using two conformations (rotated and coplanar). Distances in Å

We have also computed the asymmetric complexes using both coplanar and rotated conformations. The geometries are given in **Figure S41**. Unfortunately, the trend is opposite to the experimental behavior. That is, experimentally the Py–I,Ag distance is shorter than the dmap–I,Ag distance and theoretically the opposite trend is observed.

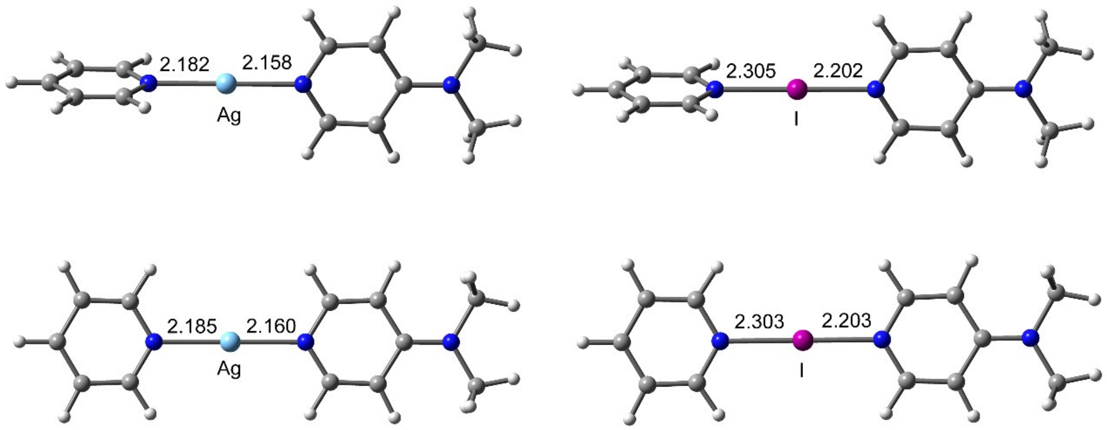

Figure S41. M06-2X/def2-TZVP optimized geometries of the asymmetric compounds using two conformations (rotated and coplanar). Distances in Å

Additionally, we have computed the HOMO and HOMO-1 in the planar conformation of the asymmetric complexes. The plots are represented in **Figure S42** (see also **Figure 5** in the main text). It is interesting to highlight that the Ag does not participates neither in the HOMO nor the HOMO-1. In contrast, the I-atom actively participates in the HOMO and HOMO-1. Moreover, the nature of the molecular orbitals is π-antibonding in the N–I bonds. This likely explains the longer N–I distances in Py–I(+)–dmap compared to the Ag–N ones in Py–Ag(+)–dmap. Moreover, in the HOMO of the iodonium complex, the pyridine ring does not participate and the I–dmap bond is antibonding in nature, thus explaining the longer I–dmap distance in the theoretical geometry.

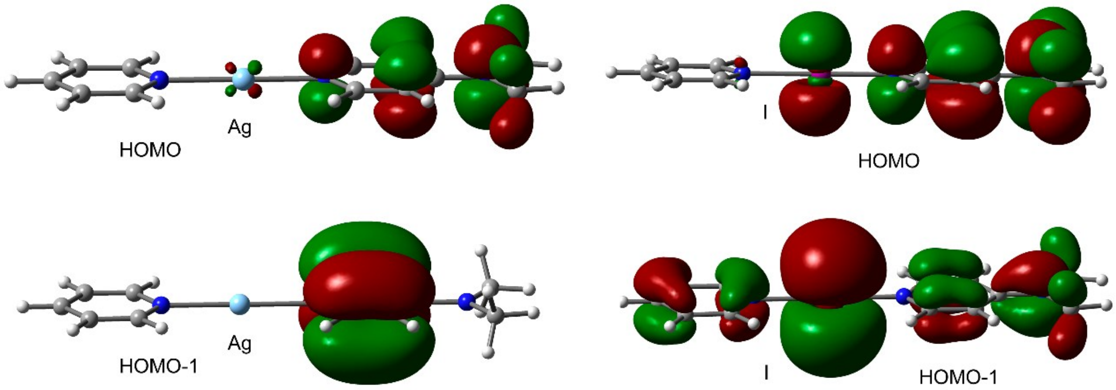

Figure S42. Plots of the HOMO and HOMO-1 of the Ag (left) and I (right) asymmetric complexes

Finally, we have studied the energy cost of enlarging the I–N(py) and Ag–N(py) distances in the asymmetric complexes. The result is shown in **Figure S43**, where in the Y-axis is represented the relative energy from the minimum and the X-axis represents the increment of the distance from the minimum. It can be observed that it is more feasible to enlarge the I(+)–N bond than the Ag(+)–N bond. Moreover, the energy cost of enlarging the distance 0.2 Å is less than 2 kcal/mol in both systems, therefore any additional force in the solid state can compensate this energy cost and provoke distortion of the N–I,Ag bond up to 0.2 Å This fact along with the π-antibonding character of the N–I bond could explain the asymmetry of the distances.

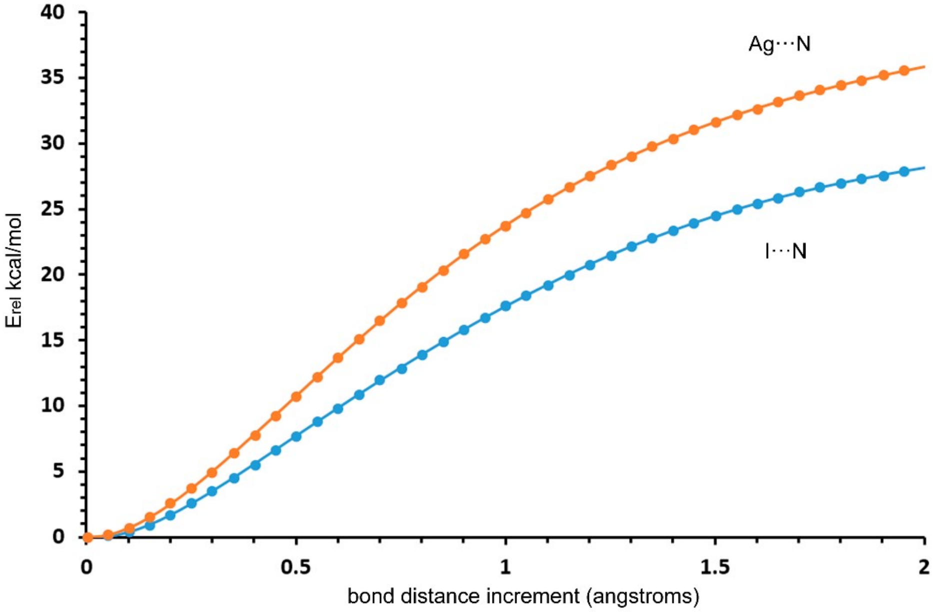

Figure S43. Plot of the relative energy (kcal/mol) versus the bond distance increment in Å in dmap–Ag(+)–py (orange) and dmap–I(+)–py (blue) distances

5. References

---

[1] C. Y. Chen, J. Y. Zeng, H. M. Lee, *Inorg. Chim. Acta*, 2006, **360**, 21-30.

[2] A. C. Carlsson, K. Mehmeti, M. Uhrbom, A. Karim, M. Bedin, R. Puttreddy, R. Kleinmaier, A. A. Neverov, B. Nekoueishahraki, J. Grafenstein, K. Rissanen, and M. Erdelyi, *J. Am. Chem. Soc.*, 2016, **138**, 9853-9863.

[3] *Nonius*, 2001, COLLECT, Nonius BV, Delft, The Netherlands.

[4] Z. Otwinowski, and W. Minor, Methods in Enzymology, New York: Academic Press, 1997, **276**, 307-326.

[5] *CrysAlisPro*, 2014, v 1.171.36.35; Agilent Technologies, Ltd, Yarton, UK.

[6] G. M. Sheldrick, *Acta Crystallogr. Sect. A*, 2008, **64**, 112-122.

[7] O. V. Dolomanov, L. J. Bourhis, R. J. Gildea, J. A. K. Howard, and H. Puschmann, *J. Appl. Crystallogr.*, 2009, **42**, 339-341.

[8] G. M. Sheldrick, *Acta Crystallogr. Sect. C*, 2015, **71**, 3-8.

[9] Y. Zhao and D. G. Truhlar, *Theor. Chem. Acc*., 2008, **120**, 215-41.

[10] F. Weigend and R. Ahlrichs, *Phys. Chem. Chem. Phys*., 2005, **7**, 3297-305.

[11] Gaussian 09, Revision B.01, M. J. Frisch, G. W. Trucks, H. B. Schlegel, G. E. Scuseria, M. A. Robb, J. R. Cheeseman, G. Scalmani, V. Barone, B. Mennucci, G. A. Petersson, H. Nakatsuji, M. Caricato, X. Li, H. P. Hratchian, A. F. Izmaylov, J. Bloino, G. Zheng, J. L. Sonnenberg, M. Hada, M. Ehara, K. Toyota, R. Fukuda, J. Hasegawa, M. Ishida, T. Nakajima, Y. Honda, O. Kitao, H. Nakai, T. Vreven, J. A. Montgomery, Jr. , J. E. Peralta, F. Ogliaro, M. Bearpark, J. J. Heyd, E. Brothers, K. N. Kudin, V. N. Staroverov, R. Kobayashi, J. Normand, K. Raghavachari, A. Rendell, J. C. Burant, S. S. Iyengar, J. Tomasi, M. Cossi, N. Rega, J. M. Millam, M. Klene, J. E. Knox, J. B. Cross, V. Bakken, C. Adamo, J. Jaramillo, R. Gomperts, R. E. Stratmann, O. Yazyev, A. J. Austin, R. Cammi, C. Pomelli, J. W. Ochterski, R. L. Martin, K. Morokuma, V. G. Zakrzewski, G. A. Voth, P. Salvador, J. J. Dannenberg, S. Dapprich, A. D. Daniels, Farkas, J. B. Foresman, J. V. Ortiz, J. Cioslowski, and D. J. Fox, Gaussian, Inc., Wallingford CT, 2009.

[12] E. D. Glendening, C. R. Landis, and F. Weinhold, *WIREs Comput. Mol. Sci.*, 2012, **2**, 1-42.

[13] R. F. W. Bader, *Chem. Rev.*, 1991, **9**, 893-928.

[14] (a) J. Contreras-García, E. R. Johnson, S. Keinan, R. Chaudret, J.-P. Piquemal, D. N. Beratan, and W. Yang, *J. Chem. Theory Comput*., 2011, **7**, 625–632. (b) E. R. Johnson, S. Keinan, P. Mori-Sanchez, J. Contreras-Garcia, A. J. Cohen, and W. Yang, *J. Am. Chem. Soc.*, 2010, **132**, 6498-6506.

[15] AIMAll (Version 13.05.06), Todd A. Keith, TK Gristmill Software, Overland Park KS, USA, 2013.

[16] R. F. W. Bader, *J. Phys. Chem. A*, 2010, **114**, 7431-7444.

[17] For a review see: H. Schmidbaur, and A. Schier, *Angew. Chem Int. Ed*. 2015, **54**, 746-784.

[18] A. Terrón, B. Moreno-Vachiano, A. Bauzá, A. García-Raso, J. J. Fiol, M. Barceló-Oliver, E. Molins, A. Frontera, *Chem Eur. J.*, 2017, **23**, 2103.

[19] B. Pinter, L. Broeckaert, J. Turek, A. Ruzicka, and F. De Proft, *Chem. Eur. J.*, 2014, **20**, 734-744.